Remote Sensing of Environment 284 (2023) 113324

Contents lists available at ScienceDirect

Remote Sensing of Environment

journal homepage: www.elsevier.com/locate/rse

Simulation of ecosystem fluxes with the SCOPE model: Sensitivity to parametrization and evaluation with flux tower observations

Egor Prikaziuk [a,*], Mirco Migliavacca [b,c], Zhongbo (Bob) Su [a], Christiaan van der Tol [a]

[a] University of Twente, Faculty of Geo-Information Science and Earth Observation (ITC), P.O. Box 217, 7500 AE, Enschede, The Netherlands
[b] European Commission, Joint Research Centre (JRC), Ispra, Italy
[c] Max Planck Institute for Biogeochemistry, Hans-Knöll-Straße 10, 07745, Jena, Germany

ARTICLE INFO

Edited by Jing M. Chen

Keywords:
SCOPE model
ERA5
ECMWF
Sentinel-3
OLCI
GPP
Vcmax
LAI
Ball-Berry slope
LE
ET

ABSTRACT

Accurate estimates of carbon, water and energy fluxes between the Earth surface and the atmosphere are crucial for enhancing our understanding of ecosystem–climate interactions. Such estimates can be made by combining remote sensing derived land surface parameters with climate reanalysis data. We analysed to what degree generic (plant functional type (PFT)-independent) satellite-derived vegetation properties and climate reanalysis data can explain land surface fluxes and to what extent the PFT-specific information extends the flux simulations. For this purpose, we used the Soil Canopy Observation, Photochemistry and Energy fluxes (SCOPE) model, which combines radiative transfer in plant leaves and vegetation canopies with photosynthesis and energy balance in a single model representation of the vegetation. We evaluated the performance of SCOPE in simulating fluxes by comparison to 63 eddy covariance sites representing 10 PFTs. We varied the sources of maximum carboxylation capacity ($Vcmax_{25}$) and BallBerrySlope values (default vs literature), the seasonality of $Vcmax_{25}$ and the meteorological forcing (locally measured and climate reanalysis). The average performance of daily flux in terms of root-mean-square error (RMSE) was 2.3 ± 0.8 μmol CO_2 m^{-2} s^{-1} (R^2 = 0.74 ± 0.12) for gross primary productivity (GPP), 24 ± 8 W m^{-2} (R^2 = 0.68 ± 0.16) for latent heat flux (λE) and 50 ± 15 W m^{-2} ($R^2$0.47±0.17) for sensible heat flux (H). The inter-site variability of the annual accumulated GPP flux was captured well with seasonally varying PFT-specific $Vcmax_{25}$ (R^2 = 0.74, RMSE = 308 g C m^{-2} yr^{-1} and bias = −68 g C m^{-2} yr^{-1}). The annual accumulated evapotranspiration (ET) was overestimated (R^2= 0.31, RMSE = 101 mm yr^{-1} and bias = 37 mm yr^{-1}), mainly in the ecosystems with subtropical Mediterranean climate, for which the soil resistance to evaporation from porous space (r_{ss}) had to be constrained from soil moisture content (SMC) or land surface temperature (LST). Overall, the study demonstrates that SCOPE model can simulate ecosystem flux with high accuracy without site-specific calibration of its parameters.

1. Introduction

The quantification of the exchanges of carbon, water and energy between the land surface and the atmosphere is relevant for many applications in Earth science including hydrology, meteorology and ecology (Baldocchi et al., 2018). At local scale, the rate of these exchanges (i.e. fluxes) are measured using flux towers (e.g. FLUXNET Pastorello et al., 2020), and at global scale satellite data-driven statistical, semi-empirical or land surface models are typically used (Beer et al., 2010; Jung et al., 2020). Recent reviews give historical overview on remote sensing for terrestrial carbon (Xiao et al., 2019; Ryu et al., 2019) and water (Zhang et al., 2016) flux.

Due to the indirect nature of the relation between remote sensing indicators and fluxes, the estimation of the latter from satellite data always requires modelling. Diagnostic models rely on external information about atmospheric and land properties, which are usually the output of other models, while prognostic models simulate atmospheric and vegetation properties internally (Huntzinger et al., 2012). In this study, we focus on diagnostic ecosystem flux modelling, which requires three types of input variables: meteorological forcing, physical properties of the soil and vegetation, and vegetation biophysical and biochemical properties that determine plant functioning.

Meteorological variables are usually obtained from atmospheric general circulation models (GCMs) driven by weather satellite and weather station data. Commonly used global climatic datasets are NCEP/NCAR (Kalnay et al., 1996), MERRA2 (Gelaro et al., 2017), ERA5 (Hersbach et al., 2020). Vegetation and soil physical variables

* Corresponding author.
E-mail address: e.prikaziuk@utwente.nl (E. Prikaziuk).

https://doi.org/10.1016/j.rse.2022.113324
Received 21 December 2021; Received in revised form 8 October 2022; Accepted 14 October 2022
Available online 25 November 2022

are usually derived from polar-orbiting satellites with moderate (Envisat (MERIS) (Bezy et al., 2000), Aqua and Terra (MODIS) (Justice et al., 2002), Sentinel-3 (Donlon et al., 2012)) or high resolution (Landsat Wulder et al. (2019), Sentinel-2 (Drusch et al., 2012)). A common way of obtaining values for the properties of soil and vegetation from radiometric measurements is by inverting radiative transfer models (Homolová et al., 2013; Verrelst et al., 2018) and retrieving vegetation structure inputs of Leaf Area Index (LAI), leaf chlorophyll content (Cab) or the fraction of absorbed photosynthetically active radiation (fAPAR), followed by the modelling of fluxes with a micro-meteorological or light use efficiency model (Zhang et al., 2005; Houborg et al., 2013). The vegetation functional response, the third diagnostic model input category, is either parametrized from structural variables empirically or based on a classification of plant functional types (PFTs). For example, Rubisco maximum carboxylation capacity ($Vcmax_{25}$), the main parameter in the classic photosynthesis model by Farquhar et al. (1980), can be estimated from Cab (Luo et al., 2019) and its seasonality is often imposed by LAI (Wang et al., 2019).

The uncertainty of model-simulated fluxes depends on both the model formulation and the accuracy of each of the three input data sources. Reported uncertainties in gross primary productivity (GPP) attributed to the uncertainty in weather forcing vary between 9 and 32% of the estimated flux (Wu et al., 2017; Jung et al., 2007). Vegetation structure inputs such as LAI vary significantly among data products (Jiang et al., 2017), and this contributes to the uncertainty of simulated fluxes as well (Liu et al., 2018). Finally, the empirical relations between vegetation structure and functioning or the tabulated values of parameters for PFTs further contribute to uncertainty in the simulation of fluxes.

More integrated models such as CUPID (Norman, 1979), SiB (Sellers et al., 1986) and SCOPE (Soil Canopy Observation of Photosynthesis and Energy fluxes) (Van der Tol et al., 2009) combine the radiative transfer and the non-radiative energy fluxes (latent heat (λE) and turbulent heat (H) exchange with the air) into a single model representation of the soil and vegetation system. The advantage of such an integrated approach is the consistent treatment of both radiative transfer and energy balance closure at all spatial aggregation levels. Hitherto this has been more theoretical than a practical advantage because a direct inversion of a coupled model as SCOPE has not been applied at large spatial scales yet. Although SCOPE has been used in studies to improve the understanding of specific aspects of radiative transfer, such as explaining the anisotropy of thermal and chlorophyll fluorescence emission (Duffour et al., 2015; Liu et al., 2015; Yang and Van der Tol, 2018; Biriukova et al., 2020), only a few studies have focused on the overall performance of the model in simulating energy balance and carbon fluxes. Wolanin et al. (2019) combined SCOPE with a machine learning approach to estimate Gross Primary Productivity (GPP) from Sentinel-2 and Landsat 8 for five cropland (CRO) sites. Pardo et al. (2018) used SCOPE forced with MODIS and MERIS LAI to simulate GPP, net ecosystem exchange, latent, sensible and ground heat flux for rapeseed. Bayat et al. (2018) used Landsat 8 optical and thermal data to constrain SCOPE simulations of GPP and λE at a grassland (GRA) site during drought. Dutta et al. (2019) proposed a SCOPE optimization framework for retrieval of biochemical parameters from flux data of CRO and deciduous broadleaf forest (DBF). Another strategy tested on Mediterranean savannah (SAV) constrained SCOPE with optical reflectance, thermal radiance and GPP flux to retrieve plant traits (Pacheco-Labrador et al., 2019).

Since mentioned works focused on single-site studies and used site-specific model adjustments, there is a need to perform a multi-site evaluation of the default SCOPE model. In this study we

1. quantify the accuracy of SCOPE-simulated fluxes,
2. determine the best performing combination of input data sources,
3. evaluate the individual contributions of meteorological, structural and biochemical (prior) input variables to the variability (in space and time) of simulated GPP and evapotranspiration (ET).

2. Materials and methods

2.1. SCOPE

SCOPE simulates four-stream radiative transfer among horizontal canopy layers, each consisting of leaves with a stochastically described distribution of orientations towards the sun and sensor (Van der Tol et al., 2009; Yang et al., 2020a). The model considers the electromagnetic spectrum from 0.4 to 50 μm, thus including both the optical and the thermal infrared domains. In comparison with well-known land surface models such as SiB (Sellers et al., 1986), ORCHIDEE (Krinner et al., 2005), CLASS (Verseghy, 2000), JULES (Clark et al., 2011; Best et al., 2011) or CLM (Dai et al., 2003), SCOPE uses a more detailed representation of the radiative transfer: apart from distinguishing between sunlit and shaded leaves, it also differentiates irradiance within these two groups of leaves depending on their orientations, which results in more accurate flux simulations (Bonan et al., 2021), but, primarily, a better simulation of satellite signals. However, the representation of the subsurface and the soil–vegetation interaction in SCOPE is less detailed.

The photosynthesis rate per leaf layer and leaf inclination class is calculated with a classic photosynthesis and stomatal conductance model (Collatz et al., 1991, 1992; Van der Tol et al., 2014), the key parameters of which are the maximum carboxylation capacity at 25 °C ($Vcmax_{25}$) and the slope of Ball-Berry equation (BallBerrySlope). Except for the $Vcmax_{25}$, which follows an exponential decline with depth in the canopy in accordance with average illumination, all photosynthesis and stomatal parameters are uniform in the whole canopy. The leaf pigment contents were assumed uniform in vertical profile as well.

The energy balance component of SCOPE is a multi-source soil-canopy model that adjusts components' temperature until the balance closes (the net radiation matches the sum of sensible, latent and ground heat flux). An aerodynamic resistance scheme is used to partition the net absorbed radiation of each leaf layer and leaf inclination class into sensible and latent heat fluxes (Verhoef and Wallace, 2000). The sensible heat flux is driven by the gradient between individual leaf temperatures and the air temperature above the vegetation (at the reference measurement height) and the aerodynamic resistance. The aerodynamic resistance depends on surface roughness, wind speed and the atmospheric stability, which, in turn, depends on the ratio of buoyancy over mechanical turbulence according to Monin–Obukhov theory (Wallace and Verhoef, 2000; Paulson, 1970). In contrast to popular single source (SEBAL (Bastiaanssen et al., 1998), SEBS (Su, 2002), METRIC (Allen et al., 2007)) and two-source (TSEB (Norman et al., 1995)) energy balance models, SCOPE does not require land surface temperature as an input variable.

Upscaling of photosynthesis and energy fluxes from leaf to canopy level is carried out by simple integration (weighted sums), where the relative contributions of sunlit and shaded leaves are calculated from the gap fractions and the relative contributions of leaf angle classes.

All default values for SCOPE input parameters used in this study can be found in Table C.6, options are presented in Table C.7. There were, however, two modifications conducted. Firstly, the effect of soil_heat_method option was modified. In the original SCOPE model soil_heat_method 2 assigns 35% of soil net radiation to ground heat flux (G). Such assumption is justified during daytime hours (Timmermans et al., 2013), but not on a daily scale, when net radiation is positive, leading to a consistently positive G and Earth heating. Therefore, we set the G value to 0 W m^{-2}, to ensure the physically realistic annual sums. Secondly, SCOPE output parameter Actot represents net leaf assimilated carbon, with leaf respiration rate (Rd) determined as a fraction of $Vcmax_{25}$: $Rd = Rdparam \cdot Vcmax_{25}$. To make Actot represent GPP we disabled leaf respiration, setting Rdparam to 0 throughout all simulations.

2.2. Sensitivity analyses

We conducted global (GSA) and local (LSA) sensitivity analyses of the SCOPE model to meteorological and biochemical input parameters. These sensitivity analyses enabled us to evaluate the effect of alternative input data sources, and their accuracy requirement (e.g. locally measured versus climate reanalysis weather forcing). Previously reported GSAs of SCOPE model focused mostly on reflectance and solar-induced chlorophyll fluorescence (Verrelst et al., 2015, 2016) or thermal emitted radiance fluxes (Prikaziuk and Van der Tol, 2019). GPP sensitivity to vegetation and soil traits was addressed by Wolanin et al. (2019), however, meteorological inputs were not considered and $Vcmax_{25}$ was parametrized as a function of leaf chlorophyll content (Cab), resulting in the overestimation of Cab importance for GPP, compared to Koffi et al. (2015). GSA for total (sum of soil and vegetation components) net radiation and λE was conducted by Jin et al. (2019), also considering a limited number of input parameters. Therefore, in our study, GSA target variables were canopy photosynthesis (GPP) and both total and individual component (soil, vegetation canopy) energy balance fluxes (λE, H, G and net radiation (Rn)). We varied optical, biochemical and meteorological parameters of the original SCOPE model; details of the GSA setup can be found in Prikaziuk and Van der Tol (2019). Briefly, the Sobol' method from SALib Python package was used for 32 input parameters and after 600,000 model runs first and total order sensitivity indices were calculated for target fluxes. The values of the most influential and at the same time incontestable meteorological parameters, incoming shortwave and longwave radiation and air temperature, were fixed to their default values of 600 W m^{-2}, 300 W m^{-2} and 20 °C, respectively.

In contrast to GSA, LSA changes one value per run (thus does not take parameter interaction into account), but shows the direction and magnitude of a target variable change. A published LSA of SCOPE for GPP used a fixed air temperature Koffi et al. (2015). Duffour et al. (2015) conducted LSA for energy balance fluxes varying only biochemical variables ($Vcmax_{25}$ and the stomatal marginal water cost of carbon assimilation); the results were presented in terms of RMSE and bias, which are rather case specific than general. LSA conducted in the present work demonstrates the effect of the temperature correction option of SCOPE on GPP, λE and H and the maximum possible simulated values of these output variables. Parameters that showed GSA total sensitivity index values higher than 0.05 were sampled within the same ranges as in GSA and used for LSA simulations. LSA was run for eight LAI classes 0.1, 0.5, 1, 2, 3, 4, 5, 6 m^2 m^{-2}.

2.3. Parametrization of SCOPE

Apart from testing the overall performance of the SCOPE model, we were specifically interested in the contribution of various model inputs to explaining the variability in measured fluxes. The configuration of SCOPE model options is presented in Table C.7, fixed input parameters are given in Table C.6, eddy-covariance site-specific parameters are listed in Table C.5, and plant functional type-specific biochemical parameters can be found in Table 1. Site-specific LAI and meteorological variables from Table 2 varied daily per site. Below we list the sources of data and motivate our choice.

2.3.1. Vegetation structure

Several polar-orbiting satellites provide global coverage at a nearly daily temporal resolution, such that multiple cloud-free images of the area of interest per year are available almost everywhere. This allows for the retrieval of time series of vegetation traits – LAI and leaf chlorophyll content (Cab) – with numerical, physical or hybrid approaches (Verrelst et al., 2018). Such time series carry uncertainty in representativeness due to varying viewing geometry among images, varying atmospheric conditions, and differences in pixel geo-location among orbits (Prikaziuk et al., 2021). As a result, additional filters and quality control metrics are required to obtain a realistic time series of retrieved surface properties. There are spatial and temporal differences between available products (Fang et al., 2013; Jiang et al., 2017), which seriously affects simulated fluxes (Liu et al., 2018). Lately the Copernicus Global Land Service LAI product has been proven to deliver high quality data (Fuster et al., 2020) and was used for global Cab quantification (Croft et al., 2020). The 10-daily smooth 300-m product combines Sentinel-3 Ocean and Land Colour Instrument (OLCI) and PROBA-V data in a Neural Network. The LAI values per site were extracted with Jupyter notebook on Terrascope platform server of VITO (VITO, 2022) and downloaded.

Local sensitivity analysis showed that the response of fluxes to Cab saturates after the value of 10 μg cm^{-2}. Cab retrieved from Sentinel-3 OLCI top of atmosphere radiance with SPART model (Yang et al., 2020b, 2021) never reached such low values, therefore Cab values were fixed to 40 μg cm^{-2} throughout the simulations.

2.3.2. Vegetation functioning

In contrast to structural vegetation traits, functional parameters, maximum carboxylation capacity of rubisco ($Vcmax_{25}$) and the Ball-Berry stomatal parameter (BallBerrySlope), do not have specific spectral signatures and cannot be directly retrieved from optical remote sensing. There are, however, various empirical parametrization schemes that can be applied.

In some studies $Vcmax_{25}$ was estimated from solar-induced chlorophyll fluorescence (SIF) (Zhang et al., 2014; He et al., 2019), but this research is still in an early stage and SIF data are not available at the spatial resolution of Sentinel-3 data. However, the upcoming ESA FLEX mission, designed for SIF estimation in tandem with Sentinel-3 (Drusch et al., 2017), may be used in the future. $Vcmax_{25}$ can also be calculated with empirical formula from leaf chlorophyll content (Luo et al., 2019) or canopy chlorophyll content expressed in MERIS terrestrial chlorophyll index (MTCI) (Alton, 2017); Sentinel-3 OLCI level-2 OLCI product is the successor of MTCI (Pastor-Guzman et al., 2020). Thermal domain data, such as land surface temperature, have theoretically been found to be useful for $Vcmax_{25}$ retrieval, but in practice, we have not been able to achieve the acceptable quality of such retrievals yet (Prikaziuk and Van der Tol, 2019).

For lack of a universal, quantitative understanding of the relation of $Vcmax_{25}$ with remotely sensed indicators, the usage of a single value of $Vcmax_{25}$ per plant functional type (PFT) remains the most popular way of the ecosystem flux model parametrization. Common $Vcmax_{25}$ per PFT data sources are the TRY database (Kattge et al., 2009) and multiple model optimization studies (Groenendijk et al., 2011; Norton et al., 2019).

We evaluated the effect of the choice of sources of $Vcmax_{25}$ and BallBerrySlope parameters alternative to the default SCOPE values of 60 μmol CO_2 m^{-2} s^{-1} and 8, respectively (Table 1). The work of Groenendijk et al. (2011) was selected because, along with $Vcmax_{25}$, the authors reported the λ parameter (the marginal water cost of carboxylation) which can be converted to the SCOPE BallBerrySlope parameter (Eq. (A.1)) The SCOPE-optimized PFT-dependent values of $Vcmax_{25}$ and BallBerrySlope were estimated from daily SCOPE simulations by minimizing root-mean-square error and the absolute value of bias simultaneously for GPP and λE (Section 3.2.5, Fig. 9).

Recent studies demonstrate that the ecosystem flux of CO_2 is simulated more accurately when $Vcmax$ values vary seasonally (Wang et al., 2019; Luo et al., 2018; Ryu et al., 2011). We scaled $Vcmax$ based on LAI so that the maximum seasonal value equals to the value in Table 1 (i.e. to $Vcmax_{25}$) (Ryu et al., 2011; Luo et al., 2018)

$$Vcmax_{LAI} = 0.3 \cdot Vcmax_{25} + 0.7 \cdot Vcmax_{25} \cdot \frac{\mathrm{LAI} - \mathrm{LAI}_{min}}{\mathrm{LAI}_{max} - \mathrm{LAI}_{min}} \quad (1)$$

The effects of the extinction coefficient, temperature correction and LAI-imposed seasonality on $Vcmax_{25}$ are shown in Fig. B.14.

Table 1
$Vcmax_{25}$ and BallBerrySlope values used for simulations. Default SCOPE plant functional type (PFT) independent values (default), values from Groenendijk et al. (2011) (table 3 therein) and PFT-optimized SCOPE values. Details on the calculation of BallBerrySlope (SCOPE) from the marginal water cost of evaporation λ used by Groenendijk et al. (2011) are presented in A.

PFT	$Vcmax_{25}$ µmol CO_2 m^{-2} s^{-1}			BallBerrySlope		
	SCOPE default	Groenendijk	SCOPE PFT-optimized	SCOPE default	Groenendijk	SCOPE PFT-optimized
CRO	60	48.6	50	8	7.6	6
GRA	60	43.3	50	8	12.8	10
ENF	60	34.3	40	8	11.6	10
MF	60	36.4	40	8	8.3	6
DBF	60	30.9	40	8	7.6	6
EBF	60	34.3	10	8	10.8	2
SAV	60	18	50	8	13.8	6
OSH	60	33.3	50	8	9	2
CSH	60	33.3	10	8	9	8
WET	60	33	20	8	9	8

Table 2
Correspondence of SCOPE, eddy covariance and ERA variables. Notice that ERA variables expressed in J m-2 must be divided by the number of seconds in the period to convert Joules to Watts: 3600 s for hourly, 86400 s for daily. satvap is a function that calculates vapour pressure from temperature T in °C $6.107 \cdot 10^{\frac{7.5T}{237.3+T}}$. SCOPE automatically converts vapour pressure deficit (VPD) into atmospheric vapour pressure (ea) in timeseries run.

Name	SCOPE	EC	unit	ERA	Unit
Input parameters					
incoming shortwave radiation	*Rin*	SW_IN_F	W m^{-2}	ssrd	J m^{-2}
incoming longwave radiation	*Rli*	LW_IN_F	W m^{-2}	strd	J m^{-2}
air temperature	T_a	TA_F	°C	t2 m −273.15	K
atmospheric vapour pressure	e_a	*satvap*(TA_F)–VPD_F	hPa	*satvap*(d2 m −273.15)	K
air pressure	p	PA_F	hPa	sp · 0.01	Pa
wind speed	u	WS_F	m s^{-1}	$\sqrt{u10^2 + v10^2}$	m s^{-1}
Output parameters					
outgoing shortwave radiation	HemisOutShort	SW_OUT	W m^{-2}	ssr–ssrd	J m^{-2}
outgoing longwave radiation	HemisOutLong	LW_OUT	W m^{-2}	str–ssrd	J m^{-2}
sensible heat flux	Htot	H_F_MDS (H_CORR)	W m^{-2}	sshf	J m^{-2}
latent heat flux	lEtot	LE_F_MDS (LE_CORR)	W m^{-2}	slhf	J m^{-2}
ground heat flux	Gtot	G_F_MDS	W m^{-2}	–	–
photosynthesis	Actot	GPP_NT_VUT_USTAR50	µmol CO_2 m^{-2} s^{-1}	–	–

2.3.3. Meteorological data

Accurate meteorological variables are crucial for flux simulations and global weather reanalysis products serve this purpose. They are indispensable for global mapping since they are the spatially continuous meteorological data source. We compared the runs using locally measured meteorology at eddy covariance stations (EC) with the runs using climate reanalysis meteorological forcing (ERA).

We used the global meteorological data distributed within the Warm Winter 2020 flux product. These values originate from ERA5-Land (earlier ERA-Interim (Berrisford et al., 2011)) hourly data from Copernicus Climate Data Store (Muños Sabater, 2019). The dataset contains values of two types — instantaneous (ready to use) and accumulations (difference with the previous time step has to be taken to obtain the daily cycle). The resulting hourly time series are averaged to daily values. The native resolution of the datasets is 9 km by 9 km. The FLUXNET team conducts de-biasing in order to better represent tower-scale values (Vuichard and Papale, 2015) (Fig. B.12). The correspondence of SCOPE and ERA5 variable names is presented in Table 2.

2.4. Validation data

The Warm Winter 2020 eddy covariance flux product (Warm Winter 2020 Team and ICOS Ecosystem Thematic Centre, 2022) across Europe was used in this study as a source of measured and reanalysis meteorological data (EC, ERA, respectively) and the validation data. We selected 63 out of 73 sites (Table C.5, Fig. 1). Eddy-covariance measurements are known to have energy balance closure errors (Wilson et al., 2002; Mauder et al., 2020), which can be corrected if ground heat flux (G_F_MDS) is available. At forty-five sites the corrected for energy balance closure latent (LE_CORR) and sensible (H_CORR) heat fluxes were present. The correction was conducted by the FLUXNET on the premise of the correct Bowen ratio (Pastorello et al., 2020). The daily variables used in this study for SCOPE parametrization and validation are listed in Table 2.

2.4.1. Model performance indicators

We evaluated the accuracy of the simulated fluxes temporally and across sites. The temporal comparison was conducted on daily data, the inter-site comparison on annual sums of data, representing 4–5 years for most of the sites. The fluxes were evaluated in terms of the coefficient of determination (R^2) root-mean-square error (RMSE) and bias (the mean of the difference between modelled and measured flux). Relative bias (rbias) and RMSE (rRMSE) were computed in relation to the range of measured values.

3. Results

3.1. Sensitivity analyses

3.1.1. Global sensitivity analysis

The global sensitivity analysis (GSA) examined the meteorological drivers (relative humidity (rH) (converted to the actual vapour pressure, e_a), air pressure (p), wind speed (u), as well as the parameters that can be retrieved from optical remote sensing (LAI, Cab) and prior literature-based inputs ($Vcmax_{25}$, BallBerrySlope) on simulated target fluxes (GPP, H, λE). Incoming shortwave and longwave radiation and air temperature were fixed to their default values of 600 W m^{-2}, 300 W m^{-2} and 20 °C, respectively. Fig. 2 shows the results of the GSA for the parameters that exceeded the total sensitivity index threshold of 0.05. The distribution of the net radiation over soil and vegetation canopy was strongly affected by LAI, which was the most important parameter for explaining both the net radiation and all energy fluxes

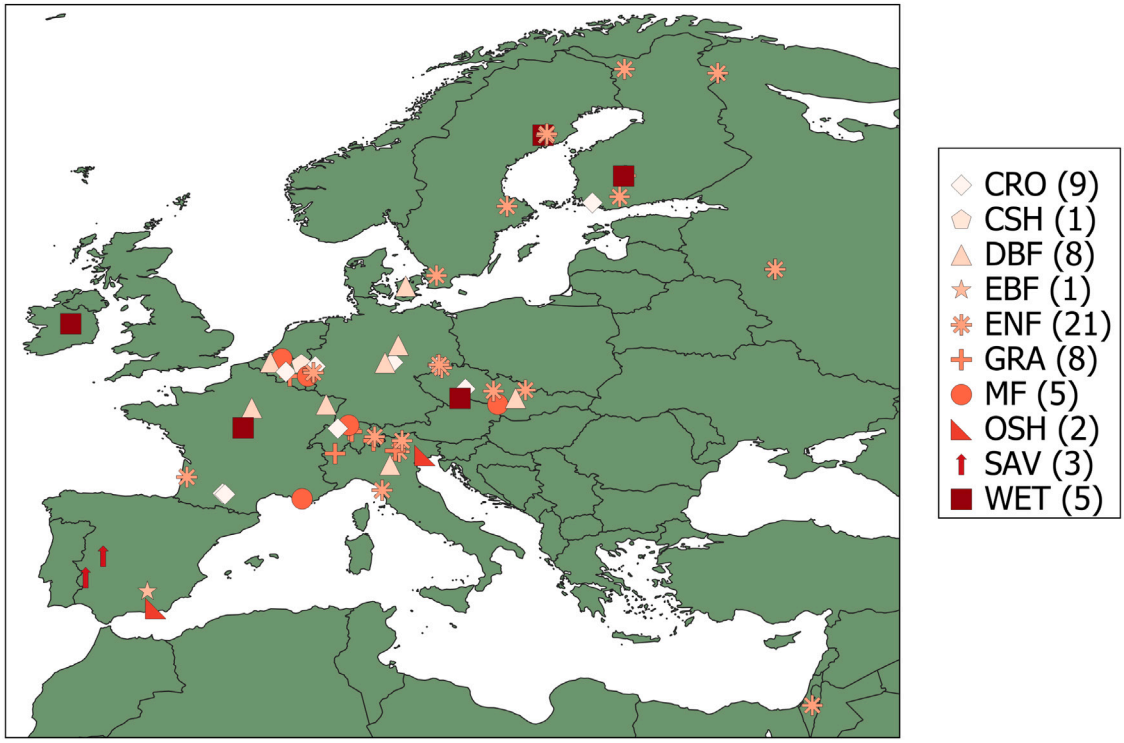

Fig. 1. 63 eddy-covariance sites from the Warm Winter 2020 eddy covariance flux product (Warm Winter 2020 Team and ICOS Ecosystem Thematic Centre, 2022) used for validation in this study.

of the soil background: sensible (H_s), latent (λE_s) and ground (G) heat fluxes (Fig. 2). Total net radiation (soil and canopy combined) revealed the influence of all studied parameters, as they all influence soil and leaf temperature and, consequently, thermal emitted radiation during the energy balance iterations. For λE_s flux the soil resistance to evaporation (r_{ss}) had as much influence than the LAI. Interestingly, the r_{ss} parameter was not equally important for the H_s flux, although the available energy is partitioned between those two fluxes. The H_c and λE_c fluxes of the canopy and the soil and canopy combined (H) were sensitive to a larger number of parameters; structural parameters of leaf (Cab) and canopy (LAI), biochemical parameters ($Vcmax_{25}$ and BallBerrySlope), and environmental parameters (p, rH). As expected, the parameter regulating stomatal conductance, BallBerrySlope, was the most important for the transpiration (λE_c). For the photosynthesis flux the influence of stomatal conductance and the carboxylation capacity was equal between each other and also equal to the sensitivity of GPP to LAI and Cab.

Note that GSA accounts for variable interactions and it calculates the impact of each variable of a complex model more precisely, but it neither reveals the direction nor the magnitude of the target variable response to changes of the input variable. The latter is demonstrated with the local sensitivity analysis (LSA) for the most influential variables according to the GSA.

3.1.2. Local sensitivity analysis

Fig. 3 illustrates the sensitivity of GPP, λE and H to the most influential biochemical ($Vcmax_{25}$, BallBerrySlope) and environmental (Rin, T_a) parameters at various levels of the structural parameter (LAI). The responses of GPP and λE were similar in terms of the direction of the parameter change (the higher — the higher). In terms of the magnitude GPP response to $Vcmax_{25}$ was larger than that of λE; GPP changed by a factor of 4 from 10 to 40 μmol m^{-2} s^{-1}, whereas λE showed a change by only a factor of 2 from 100 to 200 W m^{-2}. The situation was exactly the opposite for the response to BallBerrySlope, where the saturation of GPP was achieved at around the value of BallBerrySlope of 10, whereas the λE demonstrated an almost linear increase without any saturation. The Rin response was somewhat similar to BallBerrySlope, with saturation for GPP but not for λE. The difference in T_a response due to the temperature correction of rate coefficients and $Vcmax_{25}$ led to a decrease in GPP and λE at high and low air temperature, but the decrease in GPP was more pronounced.

The responses of λE and H were, as expected, opposite, except for Rin, the increase of which led to higher values of both λE and H.

Fig. B.15 shows the sensitivity of fluxes the other parameters: leaf chlorophyll content (Cab), soil resistance to evaporation (r_{ss}), wind speed (u), incoming longwave radiation (Rli) and actual vapour pressure (e_a). We notice that the flux values grew rapidly within the Cab range from 0 to 10 μg cm^{-2} above which the responds saturated. The high sensitivity at low chlorophyll values are responsible for the high GSA index for Cab. Because such low values of Cab are rare at the FLUXNET sites used in our study, we kept Cab fixed throughout the simulations.

3.2. Model evaluation against eddy covariance data: daily per site

The aggregated validation metrics of SCOPE-simulated fluxes on daily bases are presented in Fig. 4. The specific cases of ecosystems in Subtropical Mediterranean climate, CRO and WET are discussed in the sections below. The section concludes with the optimization scheme.

3.2.1. SCOPE performance for daily average fluxes

Fig. 4 presents the comparison metrics of daily simulated GPP, λE and H to eddy covariance measurements. The R^2 values were high: 0.75 ± 0.12 (the standard deviation among all 63 sites) for GPP, 0.67 ± 0.16 for λE, and 0.47 ± 0.17 for H. Those values did not differ significantly between the default and literature values of $Vcmax_{25}$ and BallBerrySlope. The addition of LAI-seasonality to $Vcmax_{25}$ largely reduced the RMSEs and biases for GPP and λE, making the case of PFT-specific $Vcmax_{25}$ with LAI seasonality ("Groenendijk s") the best performing: GPP RMSE = 2.3±0.8 μmol m^{-2} s^{-1}, bias = −0.2±1.0 μmol

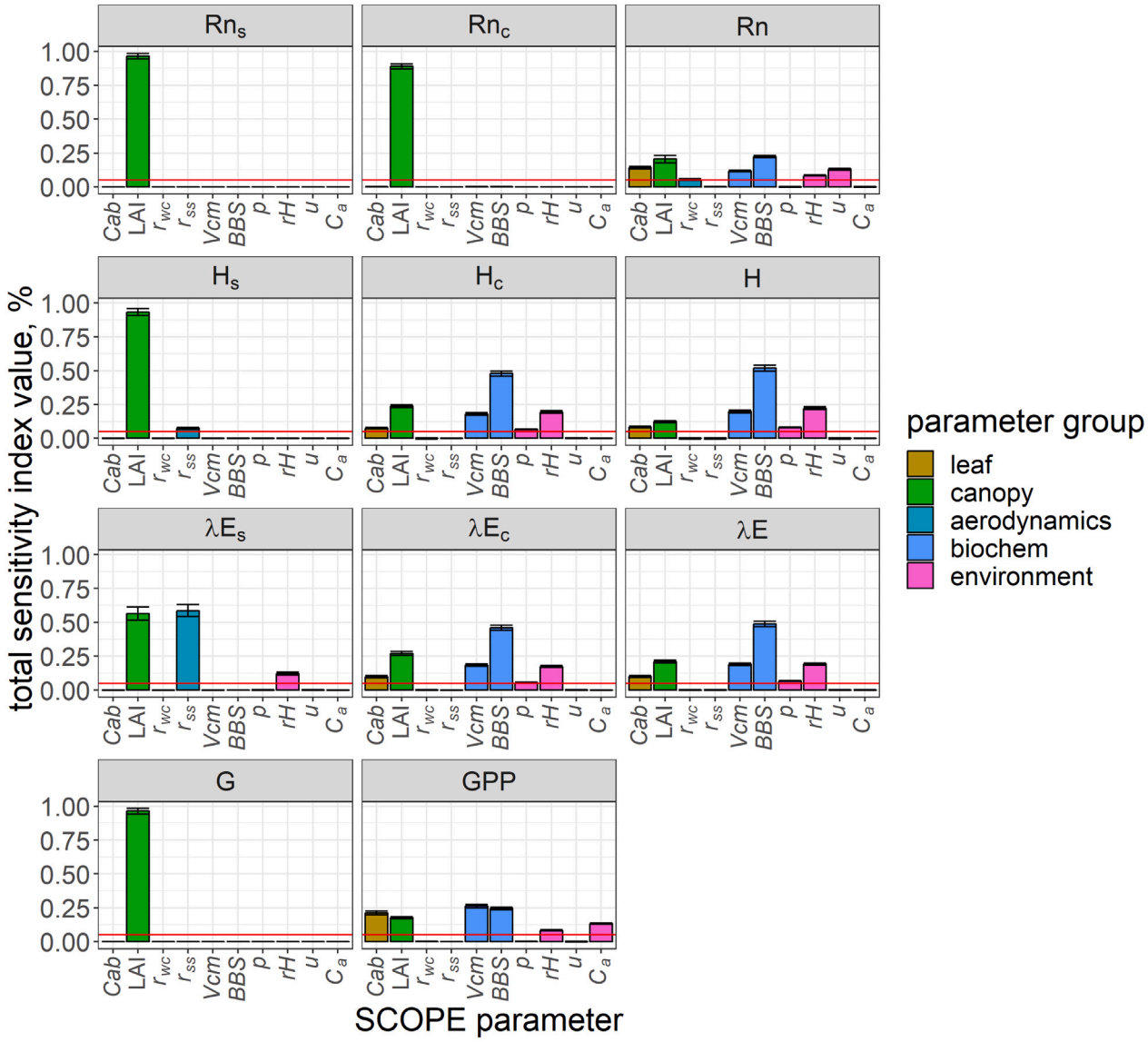

Fig. 2. Total sensitivity index values of global sensitivity analysis (GSA) of ecosystem fluxes simulated with the SCOPE model. The uncontested meteorological parameters were fixed: air temperature (T_a) to 20°C, incoming shortwave radiation (Rin) to 600 W m^{-2}, incoming longwave radiation (Rli) to 300 W m^{-2}. Subscripts: s — soil flux, left column, c — canopy (vegetation) flux, middle column. Rn — net radiation, H — sensible heat flux, λE — latent heat flux, G — ground (soil) heat flux, GPP — photosynthesis rate. Colour represents parameter group: leaf, canopy, aerodynamics, biochemical or environmental. Red line denotes 0.05 significance threshold. Parameters: leaf – Cab – leaf chlorophyll content; canopy – LAI – leaf area index; aerodynamics – r_{ss} – soil resistance to evaporation, r_{wc} — within-canopy aerodynamic resistance; biochemistry – Vcm – maximum carboxylation capacity at 25 °C ($Vcmax_{25}$), BBS — Ball-Berry slope parameter (BallBerrySlope); environment – rH – relative humidity (the proxy of e_a), p — atmospheric pressure, u — wind speed. (For interpretation of the references to colour in this figure legend, the reader is referred to the web version of this article.)

m^{-2} s^{-1}, λE RMSE = 24 ± 8 W m^{-2} bias = 4 ± 9 W m^{-2}. At the same time, the case of the default $Vcmax_{25}$ with LAI seasonality ("default s") was a bit worse: GPP RMSE = 2.9±0.9 μmol m^{-2} s^{-1}, bias 1.3±1.0 μmol m^{-2} s^{-1}, λE RMSE = 25 ± 7 W m^{-2} bias = 5 ± 10 W m^{-2}; the overestimation of the GPP flux is clear from the bias values. We optimized $Vcmax_{25}$ and BallBerrySlope values per PFT to demonstrate the peak performance of SCOPE on the dataset (see Section 3.2.5) and the values were not much better than the ones achieved with "Groenendijk s"; GPP RMSE = 2.2±0.9 μmol m^{-2} s^{-1}, bias 0±0.8 μmol m^{-2} s^{-1}, λE RMSE = 21 ± 7 W m^{-2} bias = 0 ± 8 W m^{-2}. The optimization mostly reduced biases.

PFT-wise the performance was even in terms of RMSE and bias, however, certain grouping can be observed based on the R^2 values. For GPP flux, three R^2 groups can be identified OSH, CSH with R^2 around 0.6, GRA, ENF with R^2 around 0.7 and the remaining PFTs with R^2 around 0.8. For λE, two groups are visible CRO, ENF and OSH with R^2 around 0.6 and the other with R^2 around 0.8. For H there were also two groups with low (CRO, GRA, ENF, MF, DBF) and high (SAV, OSH, CSH, WET) accuracy in terms of the R^2 and RMSE.

As far as individual sites comparison is concerned, the largest discrepancies were visible in λE and H, especially for an EBF, a site located in Subtropical Mediterranean climate zone, which is described in detail in the following section.

3.2.2. Subtropical mediterranean (drought-prone) ecosystems

Ten eddy-covariance sites were located in subtropical Mediterranean climate: 4 forests (DBF, EBF, ENF, MF), 2 OSH, 4 SAV. For most of the sites the default SCOPE simulation of λE did not match the observations during the drought period in summer (Fig. 6). Although recently SCOPE has been coupled to the hydrological model STEMMUS (Wang et al., 2021b) to address this issue, we present results for a simpler parametrization of water limitation for the ES-LM1 Mediterranean dehesa (SAV) site.

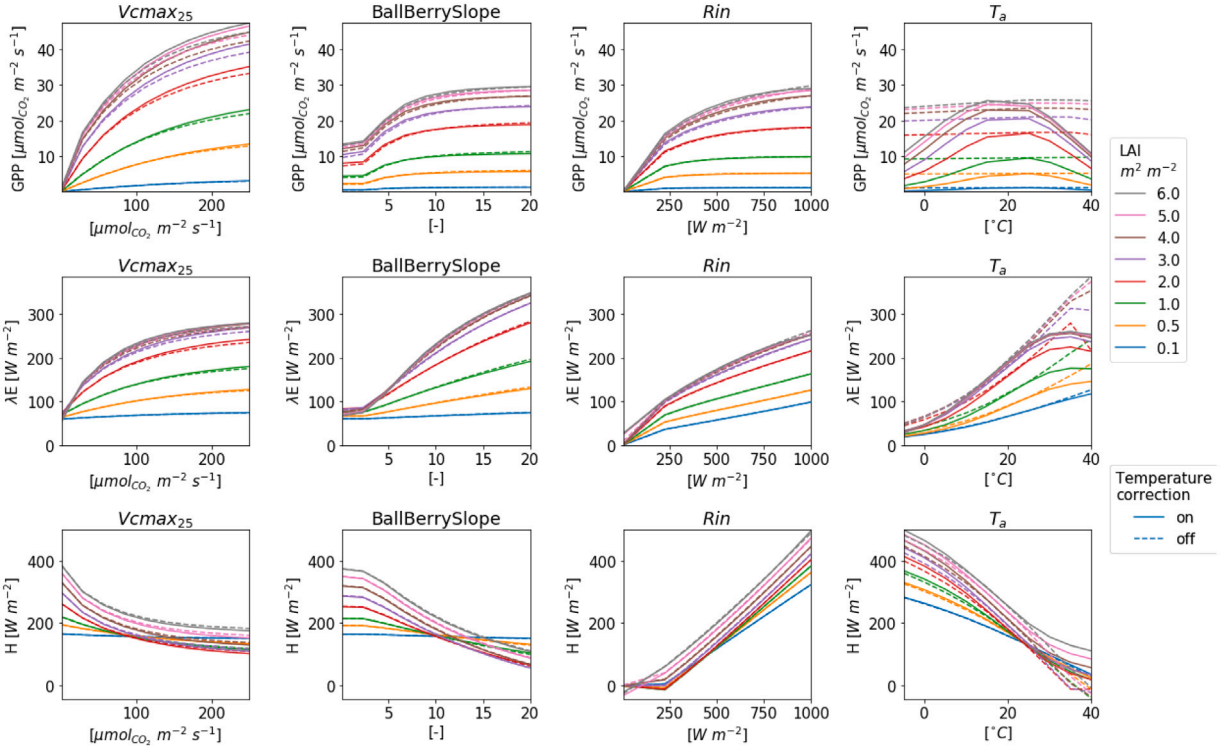

Fig. 3. Local sensitivity analysis (LSA) of SCOPE modelled fluxes at varying LAI levels (legend). Top — gross primary productivity (GPP), middle — latent heat flux (λE), bottom — sensible heat flux (H). $Vcmax_{25}$ — maximum carboxylation capacity at 25 °C, BallBerrySlope — Ball-Berry slope parameter, Rin — incoming shortwave radiation, T_a — air temperature. For LSA results for other parameters with high GSA index values see Fig. B.15.

The limitation of SCOPE to represent latent heat flux in Savannah is evident during the second half of the season (Fig. 5), when the measured flux diminishes. The transpiration flux in SCOPE can be adjusted by $Vcmax_{25}$ and BallBerrySlope, which both have a non-linear, positive effect on the latent heat flux. Compared to the default parameter values, the value for $Vcmax_{25}$ optimized by Groenendijk et al. (2011) is lower (13 versus 60 μmol m^{-2} s^{-1}) and that for BallBerrySlope higher (13.8 versus 8), with a net effect of a lower λE.

The soil λE flux in SCOPE can be adjusted by using a soil surface resistance parameter r_{ss} dependent on soil moisture (Pacheco-Labrador et al., 2019) or soil hydraulic conductivity (Bayat et al., 2019), retrieved from the thermal infrared data (Bayat et al., 2018) or modelled with a hydrological model (Wang et al., 2021b). We found that the (optional) default empirical relation of r_{ss} with SMC in SCOPE, notably $r_{ss} = \max(11.2 \cdot \exp(42 \cdot (0.22 - SMC)), 500)$ already improves the simulation of λE (Fig. 6), but a more physically based approach would require parametrization based on soil hydraulic properties (Van de Griend and Owe, 1994). For this reason we did not use a soil moisture dependent r_{ss} at sites which are not located in the subtropical Mediterranean climatic zone. An alternative method of r_{ss} retrieval from land surface temperature (LST) data is presented in the Appendix B.5

3.2.3. Cropland

For croplands (CRO), the field size with respect to the eddy-covariance fetch and the satellite pixel resolution, crop rotation (Bégué et al., 2018) and crop management require consideration. Most fields around the sites in this study are small (an average European Union field is 16 ha (Eurostat) of greatly varying shape). Since we were using Sentinel-3 OLCI sensor with the nominal resolution of 300 m and the effective resolution of 700 m (Prikaziuk et al., 2021), we did an additional check that the pattern of the Sentinel-3-retrieved LAI coincides with the pattern of Sentinel-2 LAI from Copernicus high resolution vegetation phenology (HR-VPP) product (Tian et al., 2021) (Fig. 7).

Legislation stipulates crop rotation but the identification of crop and fallow is a challenging task and often requires satellite data of high spatial resolution. We concentrated on the FR-Lam site for which the crop rotation scheme has been published (CESBIO, 2022): irrigated winter wheat (C3) and corn (C4). Indeed we observed high values of GPP in 2019 (30 μmol m^{-2} s^{-1}) when corn was planted (Fig. 8). To accommodate the photosynthetic pathways in the SCOPE simulations, we ran the time series for both C3 and C4 sub-models with the corresponding (default) parameters but this did not improve neither GPP nor λE.

3.2.4. Wetlands

WET was the best case for λE estimation, probably due to the absence of any water stress (Fig. B.16). The accuracy of GPP simulations was latitude-dependent: for the northern sites in Sweden (SE-Deg) and Finland (FI-Sii) GPP was largely overestimated. In these boreal wetlands, root zone water temperature may limit metabolism even if air temperatures rise: The measured values did not exceed 3 and 5 μmol m^{-2} s^{-1} for SE-Deg and FI-Sii, respectively. For central European sites (CZ-wet, FR-LGt) the range of measured GPP values reached 10 μmol m^{-2} s^{-1}, of simulated — 15 μmol m^{-2} s^{-1}.

3.2.5. Optimal parametrization

The $Vcmax_{25}$ and BallBerrySlope parameters could be calibrated to measured GPP and λE fluxes, but for each of these fluxes separately the problem is ill posed. Fig. 9 shows that the minima in RMSE can be found for the pairs of $Vcmax_{25}$ and BallBerrySlope. In this particular case of MF, Groenendijk values (green star) were closer to the optimum SCOPE parametrization (orange start) than the default ones (yellow star). Yet, for many PFTs both the default and Groenendijk values differed considerably from the optimized values (Table 1). The coefficient of determination for the daily flux simulations is driven by the seasonality of meteorological and LAI data thus it varied little over the whole $Vcmax_{25}$-BallBerrySlope parameter space.

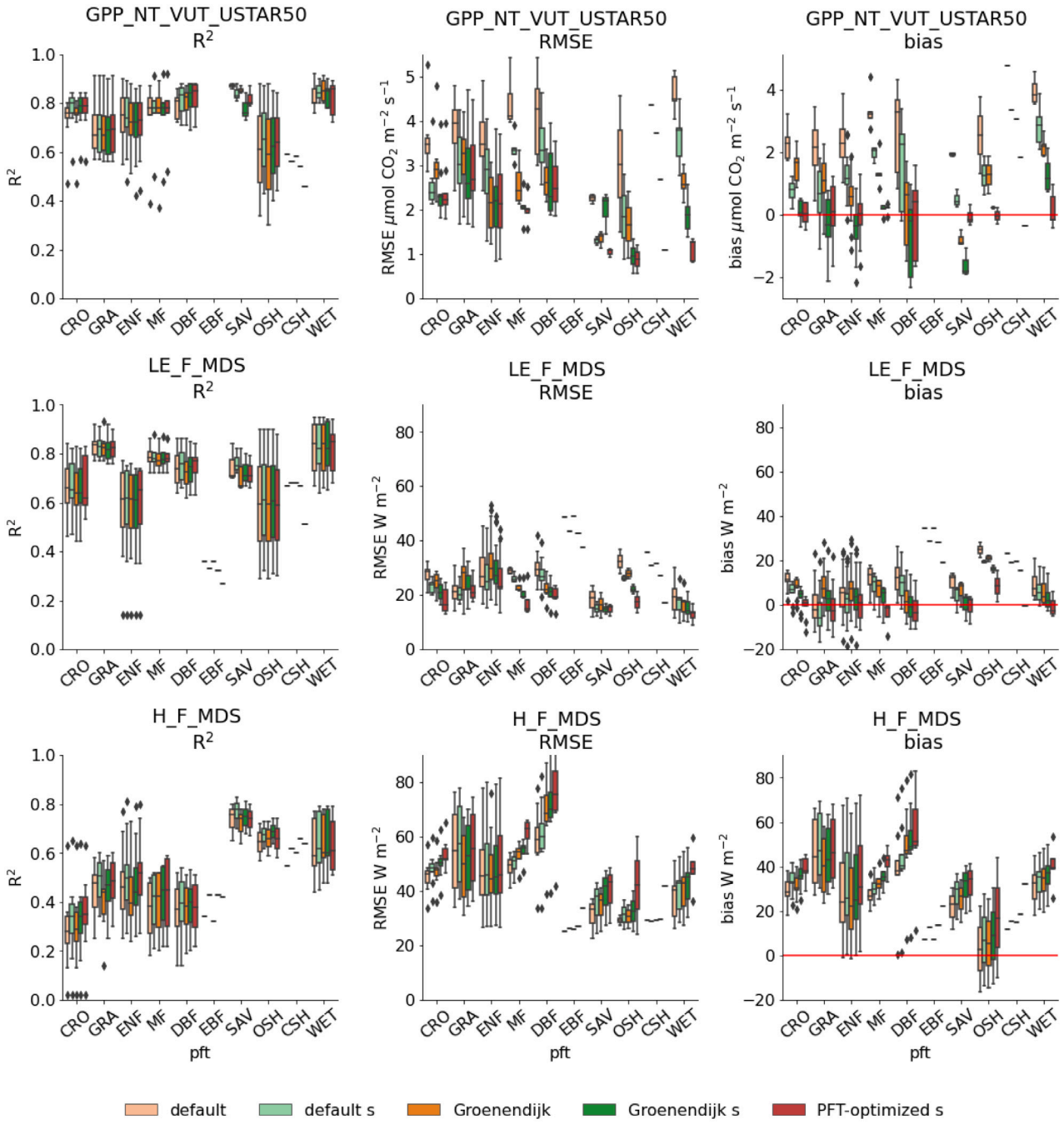

Fig. 4. Performance metrics of SCOPE-simulated daily GPP (top row), λE (middle row), and H (bottom row). SCOPE was parametrized with daily average eddy covariance meteorological data (EC) and default, Groenendijk or SCOPE PFT-optimized $Vcmax_{25}$ and BallBerrySlope values (see Table 1): "s" denotes the cases when LAI-seasonality was added to $Vcmax_{25}$ ($Vcmax_{LAI}$). Red line denotes the target level of bias.

3.3. Model evaluation against eddy covariance data: annual across sites

Fig. 10 shows the inter-site correlation of SCOPE simulated annual sums of GPP and ET, parametrized with mean per PFT $Vcmax_{25}$ and BallBerySlope from Groenendijk et al. (2011) and meteorological data measured at eddy covariance tower (EC). The ecosystems form clusters that are especially well seen in GPP (top row). One outlier is visible for λE, in ES-Cnd, EBF, due to water limitation on soil evaporation that was not well represented with the default representation of r_{ss} versus SMC. The addition of LAI seasonality to $Vcmax_{25}$ reduced the bias and RMSE of GPP and λE simulation. SCOPE-simulated values showed a higher coefficient of determination and lower RMSE and the absolute value of bias when compared against the λE corrected for the energy balance closure error of the measurements (LE_CORR).

Table 3 compares the alternative parametrization options. We see that PFT-specific biochemical values outperformed the default SCOPE values in both seasonally static and seasonally varying $Vcmax_{25}$. Compared to using locally measured meteorology (EC), the use of climate reanalysis meteorological ERA5-land data did not worsen the simulation results.

3.4. Scenario analysis

In order to show the individual contribution of input parameters to the simulated fluxes, we conducted a set of simulations described in

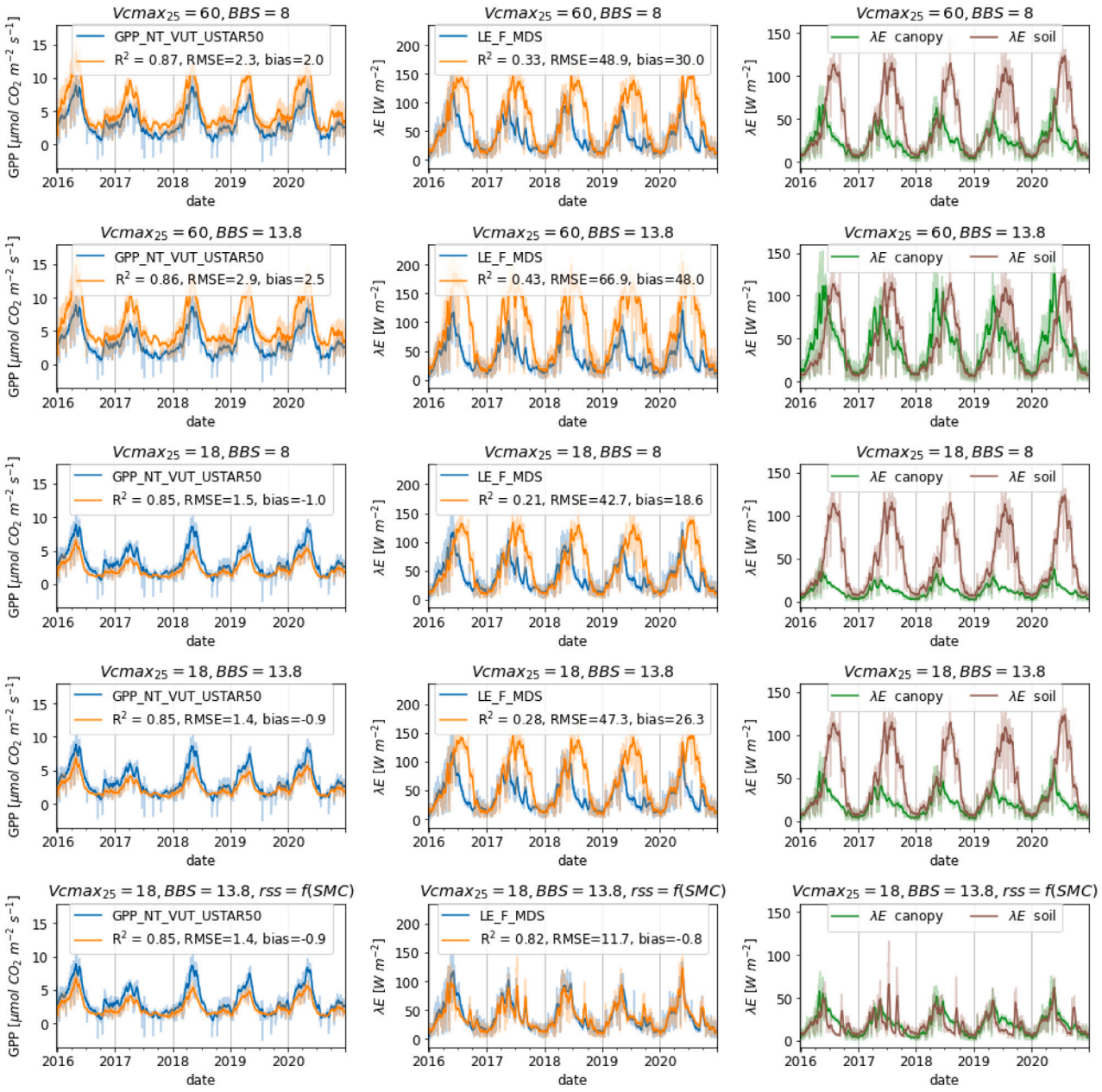

Fig. 5. The individual contributions of $Vcmax_{25}$, BallBerrySlope (BBS) and r_{ss} onto GPP and λE fluxes in the example of Mediterranean dehesas (SAV) ES-LM1 site. Left column — GPP, middle column — total λE, right column — λE components: λE canopy (transpiration) and λE soil (evaporation). Blue — eddy covariance data, orange, brown and green — modelled value, shading — real data, line — 15-day moving average. (For interpretation of the references to colour in this figure legend, the reader is referred to the web version of this article.)

Table 4 and compared the predictions with the measured values at the annual scale across sites. The initial bench-marking "naive" scenario (#1) was the run on the mean seasonal cycle of meteorological data and average LAI. In the second and third scenario's, the observed values of one of the components (LAI (#2) or meteorology (#3)) were taken into account, and in the fourth, both predictors together (LAI + meteorology (#4)). In the final scenarios, the PFT-optimized values of $Vcmax_{25}$ and BallBerrySlope were used without (#6) and with (#7) the LAI-driven seasonality of $Vcmax_{25}$. The results are presented in Figs. 11, B.18.

For GPP flux the "naive" scenario resulted in the RMSE of around 1150 g C m^{-2} yr^{-1} and the R^2 of 0.72. The inclusion of LAI (#2) decreased the RMSE by 200 g C m^{-2} yr^{-1}, the inclusion of meteorological data (#3) reduced the metric only by 150 g C m^{-2} yr^{-1}, which shows higher influence of LAI seasonality onto GPP. The substantial improvement in the simulation performance was achieved when the seasonality of $Vcmax_{25}$ (#5, #7) and PFT-dependency (#6, #7) were considered. When $Vcmax_{25}$ was kept constant RMSE was 859 g C m^{-2} (#4) or 425 g C m^{-2} (#6). When $Vcmax_{25}$ seasonality was driven by LAI RMSE went down to 503 g C m^{-2} yr^{-1} (#5) or 308 g C m^{-2} yr^{-1} (#7).

The ET flux was evaluated both against the uncorrected and the energy balance closure corrected versions of the field data. The initial "naive" simulation had a moderate performance with the RMSE of 179 mm yr^{-1} (R^2 = 0.30) for the uncorrected flux and the RMSE of 121 mm yr^{-1} (R^2 = 0.61) for the corrected flux. Similarly to the GPP flux, the inclusion of LAI (#2) resulted in a larger improvement of the simulations than the inclusion of the actual meteodata (#3); for uncorrected flux RMSEs of #2 was 144 mm yr^{-1} (R^2 = 0.28), of #3 was 165 mm yr^{-1} (R^2 = 0.29), for corrected flux RMSEs of #2 was 101 mm yr^{-1} (R^2 = 0.56), of #3 was 107 mm yr^{-1} (R^2 = 0.62).

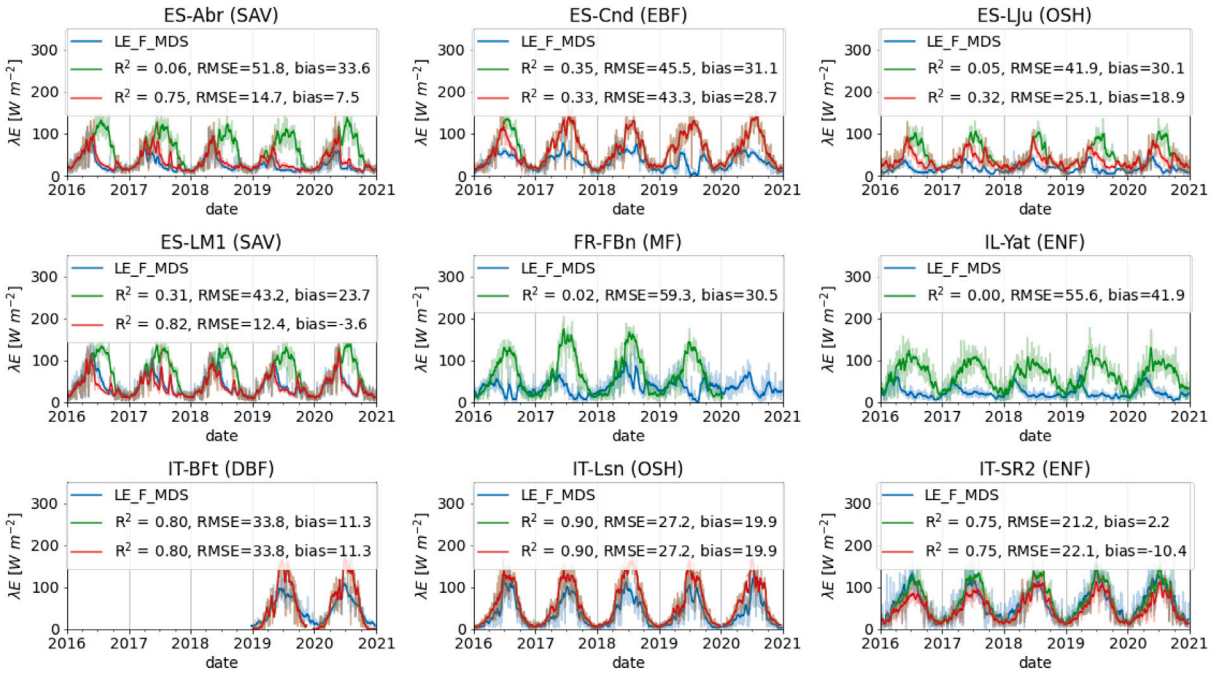

Fig. 6. Simulations of λE flux for sites in subtropical Mediterranean climate. Blue — measured flux, green — default $Vcmax_{LAI}$ case, red — default $Vcmax_{LAI}$ case with r_{ss} computed from soil moisture content, where it was available. Shading — real data, line — 15-day moving average. (For interpretation of the references to colour in this figure legend, the reader is referred to the web version of this article.)

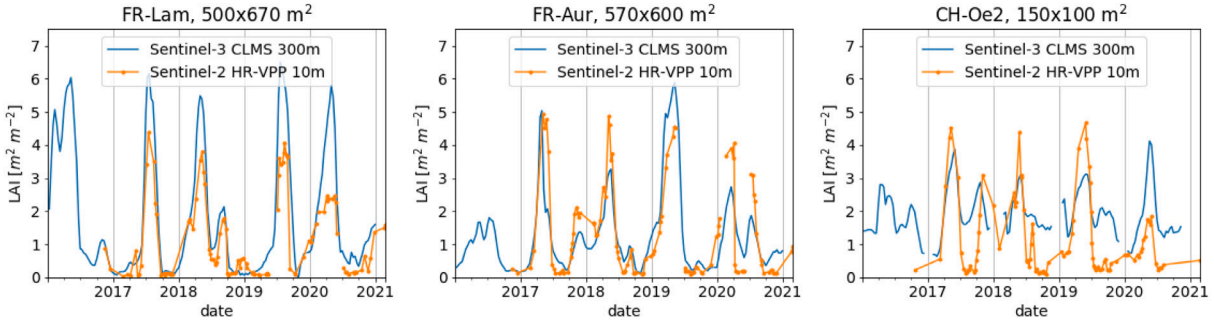

Fig. 7. The effect of the field size onto the retrieved LAI. Blue line — LAI from Sentinel-3 (1 pixel), orange line — LAI from Sentinel-2, average of all pixels within the field boundary. CH-Oe2 (right) is the smallest field in our dataset. (For interpretation of the references to colour in this figure legend, the reader is referred to the web version of this article.)

Table 3
The effect of various $Vcmax$ and meteorological data sources on SCOPE-simulated annual sums of GPP and ET. Numbers in bold represent the best case. For ET the uncorrected flux (LE_F_MDS) was used.

	GPP g C m^{-2} yr^{-1}				ET mm yr^{-1}			
	R^2	RMSE	rRMSE	bias	R^2	RMSE	rRMSE	bias
EC								
Vcmax static ($Vcmax_{25}$)								
default	**0.73**	859	0.30	792	0.30	136	0.27	86
Groenendijk EC	0.71	**425**	**0.15**	**273**	**0.36**	**125**	**0.25**	**75**
Vcmax seasonal ($Vcmax_{LAI}$)								
default	**0.74**	503	0.18	397	0.27	111	0.22	50
Groenendijk EC	**0.74**	**308**	**0.11**	−68	**0.31**	**101**	**0.20**	**37**
ERA								
Vcmax static ($Vcmax_{25}$)								
default ERA	**0.74**	866	0.30	800	0.29	165	0.33	100
Groenendijk ERA	0.71	**427**	**0.15**	**275**	**0.33**	**153**	**0.30**	**90**
Vcmax seasonal ($Vcmax_{LAI}$)								
default ERA	**0.75**	500	0.17	396	0.28	137	0.27	64
Groenendijk ERA	0.74	**307**	**0.11**	−71	**0.30**	**125**	**0.25**	**52**

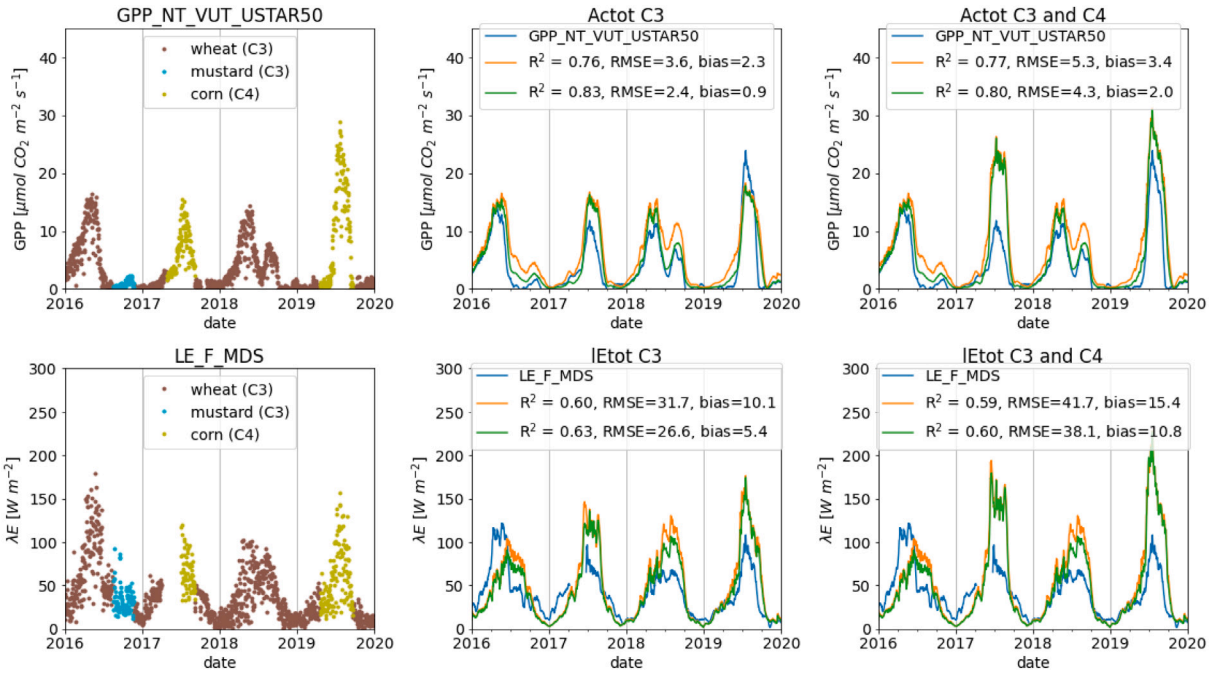

Fig. 8. The effect of the C3-C4 crop rotation in the example of FR-Lam field. Blue — eddy covariance flux, orange — default $Vcmax_{25}$ case, green — default $Vcmax_{LAI}$ case. Line — 15-day moving average. (For interpretation of the references to colour in this figure legend, the reader is referred to the web version of this article.)

Table 4
Scenario definitions.

#	scenario	meteo	LAI	$Vcmax_{25}$ BallBerrySlope
1	naive	mean seasonal	mean	default
2	+ LAI	mean seasonal	S3-retrieved	default
3	+ meteo	EC-measured	mean	default
4	+ meteo + LAI	EC-measured	S3-retrieved	default
5	+ meteo + LAI + seasonality	EC-measured	S3-retrieved	default s
6	+ meteo + LAI + $opt_{Groenendijk}$	EC-measured	S3-retrieved	Groenendijk
7	+ meteo + LAI + $opt_{Groenendijk}$ + seasonality	EC-measured	S3-retrieved	Groenendijk s
8	+ meteo + LAI + opt_{PFT} + seasonality	EC-measured	S3-retrieved	PFT-optimized s
9	+ meteo + LAI + opt_{site} + seasonality	EC-measured	S3-retrieved	site-optimized s

The addition of PFT-dependence (#4 → #6) improved the simulations when compared to the ET but worsened it when compared to the ET CORR. Further addition of the $Vcmax_{25}$ seasonality (#4 →#5, #6 →#7) reduced the R^2 by 0.05 but also reduced the RMSE, with a more pronounced improvement (20 mm yr^{-1} RMSE reduction) for the uncorrected flux.

Overall, the scenario analysis demonstrated that the most complete case (#7 PFT-specific $Vcmax_{25}$ and BallBerrySlope with seasonally varying $Vcmax_{25}$) demonstrated the highest accuracy for both GPP and ET, but not for the ET CORR where the default PFT-independent cases (#4, #5) performed better. It has to be noted that among 63 selected validation sites only 45 had the corrected ET.

Cases #8 and #9 demonstrate the best possible dataset-fitted performance. The PFT-fitted values (#8) presented in Table 1 may be considered SCOPE-optimized, as opposed to the Groenendijk values, which were optimized for a different model. The site-fitted values (#9) yielded the peak performance of the SCOPE model after calibration of the $Vcmax_{25}$ and BallBerrySlope parameters. Both optimizations where performed with seasonally-varying $Vcmax_{25}$.

4. Discussion

4.1. Comparison to existing models and datasets

In this study, we evaluated the performance of SCOPE model simulated carbon and energy fluxes against 63 European eddy-covariance sites in 10 PFTs. We searched for the most successful (in terms of R^2, RMSE and bias) model parametrization at the daily and yearly scales, to obtain a better understanding of the roles of remote sensing derived LAI, meteorological forcing and ancillary input of carboxylation capacity and stomatal regulation as parametrized with the BallBerrySlope. The vegetation structure parameter (LAI) and meteorological parameters were derived from Earth observation data and we varied functional parameters $Vcmax_{25}$ and BallBerySlope according to values reported in the literature. The best performing combination was the mean per PFT values reported by Groenendijk et al. (2011) with LAI-imposed seasonality: daily GPP R^2 = 0.74 ± 0.12, RMSE = 2.4 ± 0.8 g C m^{-2} d^{-1} and bias = -0.2 ± 1.0 g C m^{-2} d^{-1}, yearly sum GPP R^2 = 0.74, RMSE = 308 g C m^{-2} yr^{-1} and bias = −68 g C m^{-2} yr^{-1}, daily ET R^2 = 0.68 ± 0.16, RMSE = 0.84 ± 0.29 mm d^{-1} and bias = 0.13 ± 0.33 mm d^{-1}, yearly sum ET R^2 = 0.31, RMSE = 101 mm yr^{-1} and bias = 37 mm d^{-1}.

Direct comparison of different models is complicated due to differences in model architecture and the underlying assumptions, and in the spatial and temporal resolutions of the input parameters. For example, SCOPE as an energy balance model does not use land surface temperature as input, in contrast to the Two-Source Energy Balance model (TSEB) (Kustas and Norman, 1999). In contrast to hydrological models, SCOPE soil water balance is constrained only by energy availability, but not by root zone water availability. Photosynthesis flux is simulated by Collatz et al. (1991, 1992) modification of the classic Farquhar et al.

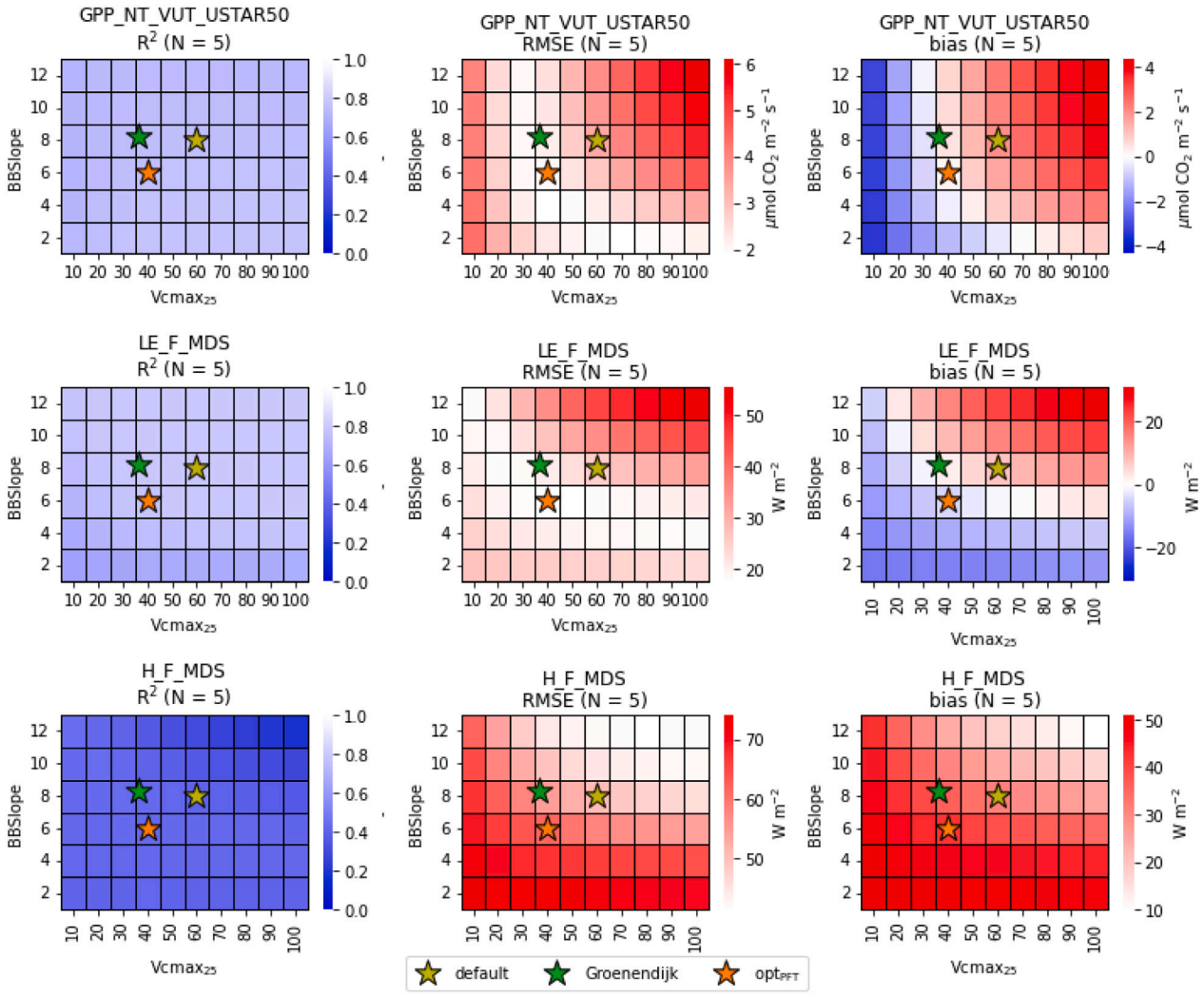

Fig. 9. The shape of the metric loss-function in the $Vcmax_{25}$-BallBerrySlope parameter space for mixed forest (MF) ecosystems. Top row — GPP, middle row — λE, bottom row — H. Left column — R^2, middle column — RMSE, right column — bias; all metrics are averages per 5 MF sites. Yellow star — default parametrization, green star — Groenendijk parametrization, orange star — SCOPE PFT-optimized parametrization (Table 1). All simulations were done with seasonally dynamic $Vcmax_{LAI}$. The whiter — the better. Please, notice that the colorbar ranges of RMSE and bias for λE and H are not aligned. (For interpretation of the references to colour in this figure legend, the reader is referred to the web version of this article.)

(1980) model, whereas Light Use Efficiency (LUE) model by Monteith (1972) is also widely used for satellite products, for example by the MODIS team (Running and Mu, 2019). Spatial resolution in this study was determined by the Sentinel-3 OLCI pixel size with the nominal value of 300 m and the actual footprint of 700 m (Prikaziuk et al., 2021), the temporal resolution was daily and annual. Acknowledging that these model representations vary, we compare SCOPE performance metrics to that of other models.

Boreal Ecosystem Productivity Simulator (BEPS) (Chen et al., 1999) simulations for 2000–2005 have been compared to MODIS and 40 Eddy covariance sites earlier (Zhang et al., 2012). The reported annual RMSE for MODIS was 457 g C m^{-2} yr^{-1} (R^2 = 0.44), for BEPS 347 g C m^{-2} yr^{-1} (R^2 = 0.68). $Vcmax_{25}$ values for this study were taken from Kattge et al. (2009). The Breathing Earth System Simulator (BESS) (Ryu et al., 2011) global maps for 2001–2015 have been compared to 113 Eddy covariance sites, MODIS ET (Running et al., 2019) and GPP (Running and Mu, 2019) products and benchmarked against Max–Planck institute for biogeochemistry (MPG) GPP and ET products (Jung et al., 2011) by Jiang and Ryu (2016). The overall 8-day metrics were very similar to the daily values reported in our work: MODIS GPP R^2 = 0.59, RMSE = 2.86 g C m^{-2} d^{-1}, ET R^2 = 0.52, RMSE = 0.86 mm d^{-1}, BESS GPP R^2 = 0.67, RMSE = 2.58 g C m^{-2} d^{-1}, ET R^2 = 0.62, RMSE = 0.78 mm d^{-1}. Mean annual sums of MODIS and BESS data demonstrated negative bias (underestimation) of GPP of approximately −150 g C m^{-2} yr^{-1} (MODIS R^2 = 0.57, BESS R^2 = 0.52), whereas SCOPE simulations of GPP were less biased and the coefficient of determination was higher. MODIS and BESS also underestimated the ET flux by −70 mm yr^{-1} (MODIS R^2 = 0.41, BESS R^2 = 0.51), whereas SCOPE overestimated it.

The advantage of SCOPE, BEPS and BESS is their independence from the measured fluxes, i.e. the measured flux is not used for their calibration and thus measured fluxes can be used for the validation of the simulated fluxes. The ability of SCOPE, BEPS and BESS to use satellite data instead makes the models applicable at larger scales. At the same time, all these models require more computational time than statistical models, and prior knowledge of soil and vegetation parameters, the most important of which for the mentioned models is $Vcmax_{25}$ and the parametrization of stomata. A large number of studies acquired $Vcmax_{25}$ values from different sources: from leaf scale measurements (Kattge et al., 2009), from solar-induced fluorescence (He et al., 2019), from thermal radiance (Pacheco-Labrador et al., 2019; Bayat et al., 2018), from statistical correlation with leaf chlorophyll content (Croft et al., 2017), from measured GPP flux (Alton, 2017), from optimality hypothesis (Walker et al., 2017; Jiang et al., 2020).

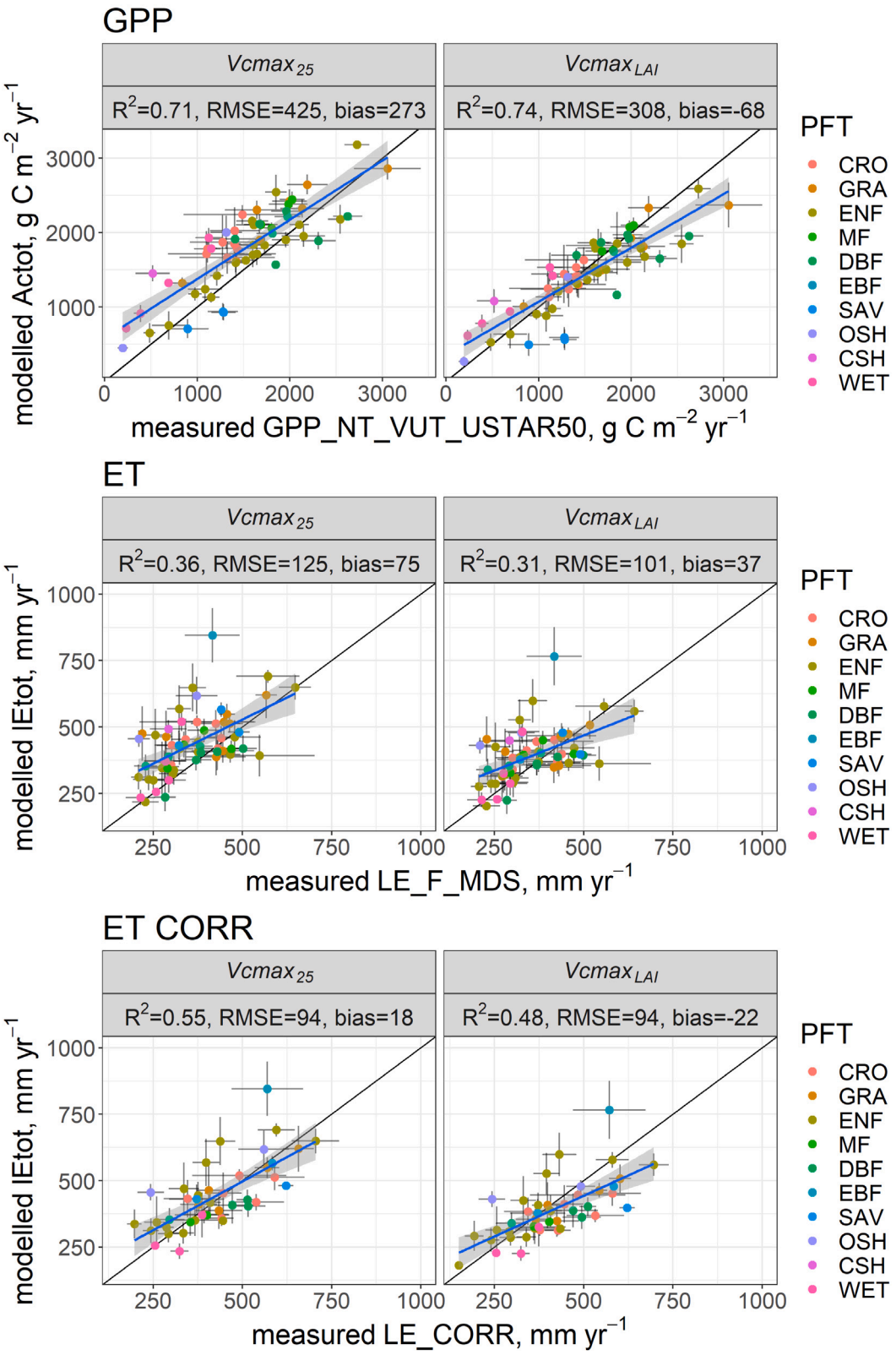

Fig. 10. Performance metrics of SCOPE-simulated annual sums of GPP and ET (variability across sites). SCOPE was parametrized with daily average eddy covariance meteorological data and Groenendijk PFT-dependent values (see Table 1). Top row — GPP, middle row — ET calculated from LE_F_MDS value, bottom row — ET calculated from LE_CORR value. Left column — simulations with static $Vcmax_{25}$ values, right column — simulations with seasonally varying $Vcmax_{LAI}$.

In this study, we avoided the calibration of $Vcmax_{25}$ to flux measurements, although the inversion framework to do so with SCOPE was developed by Dutta et al. (2019).

Several studies have used solar-induced fluorescence (SIF) in addition to or instead of the multi-spectral reflectance to estimate the GPP flux, and in a recent study, the possibility of the use of SIF for

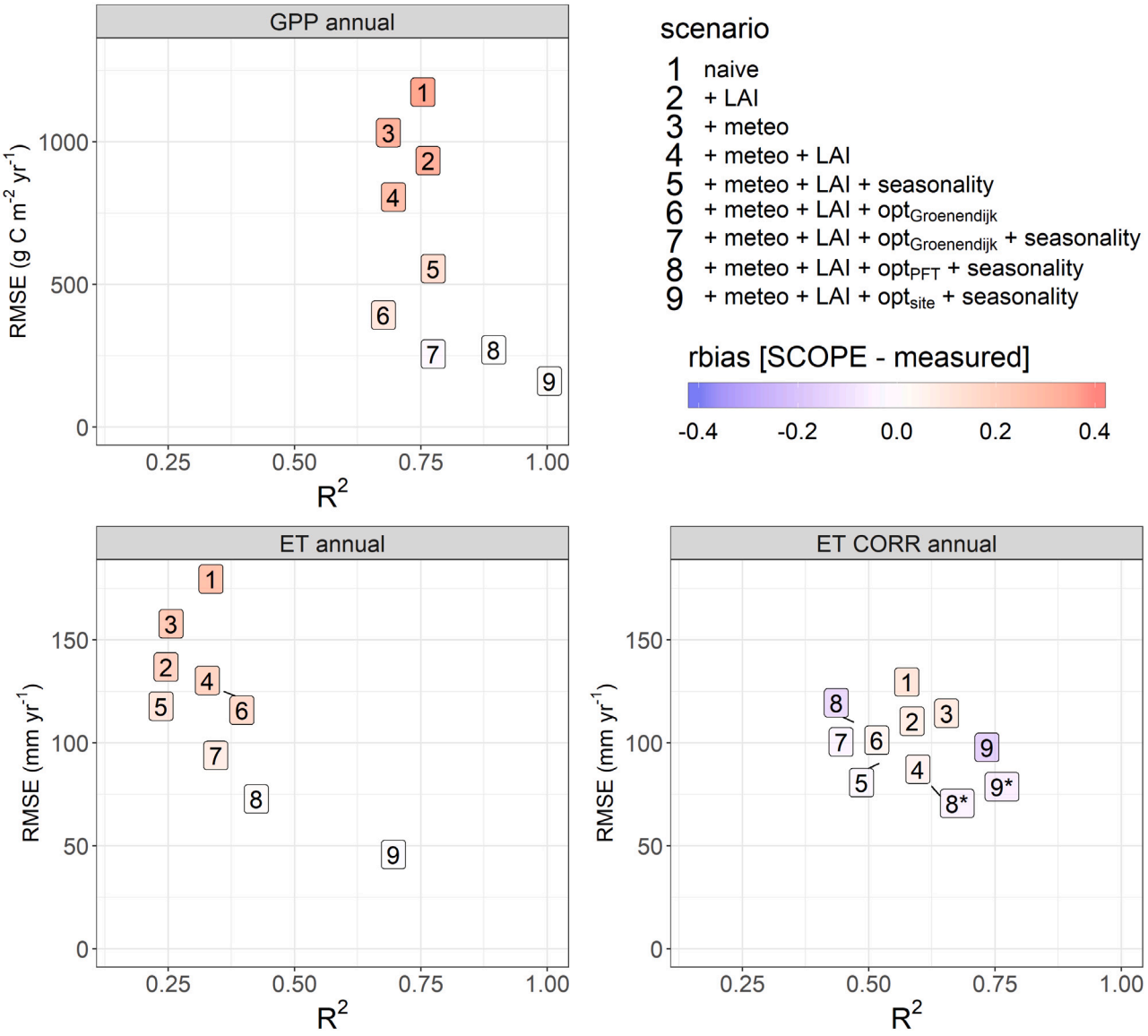

Fig. 11. Performance of the SCOPE model in various scenarios in terms of R^2 (x-axis) and RMSE (y-axis) of the annual accumulated GPP and ET fluxes (ET CORR — measured ET flux, corrected for energy balance closure, LE_CORR, ET — measured, uncorrected, computed from LE_F_MDS). The best model (lowest RMSE, highest R^2) would be located in the bottom right corner. Scenario description can be found in Table 4, the numbers correspond to the increase in input complexity. 8* and 9* are scenarios optimized for ET CORR flux. The exact values of bias can be found in Table 3. A Taylor plot for the same data is shown in Fig. B.18.

transpiration has been investigated (Maes et al., 2020). Fluorescence originates from the light-harvesting complexes in plants (Mohammed et al., 2019). The measured signal of SIF depends on illumination, absorption, the efficiencies of the subsequent energy dissipation, and scattering in the canopy. The dependence of SIF on energy dissipation efficiencies is the cause of the its relation with $Vcmax_{25}$ (Zhang et al., 2014), but the slope of GPP-SIF relationship is PFT-specific (Koffi et al., 2015), structure-dependent (Migliavacca et al., 2017; Zhou et al., 2020) and environment-dependent (Zhou et al., 2020). Wang et al. (2021b) showed that the non-linear relationship of GPP and SIF was affected by water stress. However, SIF data have a substantially lower spatial or temporal resolution than reflectance data, and most available products require temporal aggregation to reduce noise. The validation of the SIF-derived maps of GPP against 91 eddy covariance sites (Li and Xiao, 2019) resulted in lower RMSE 1.92 g C m^{-2} d^{-1} (R^2 = 0.75) than the one reported in this study. Although these SIF-GPP relations have been calibrated to field measurements, such studies demonstrate that SIF can be used to further constrain the structural or photosynthetic parameters of SCOPE. At the field level, half-hourly time series of hyperspectral optical reflectance data showed promising results for the GPP prediction with partial least squares regression (PLSR) as well (Dechant et al., 2019). Again, a comparison of performance is not meaningful, since a portion of the data was used for training.

The models based on the optimality theory is another group of models that do not require $Vcmax_{25}$ or g_s values as input, but rather infer those parameters from environmental variables (Smith et al., 2019; Harrison et al., 2021). For example, the P-model (Prentice et al., 2014; Stocker et al., 2020) uses Farquhar et al. (1980) model and applies the coordination hypothesis that the carboxylation-limited and light-limited photosynthesis are equal. The optimality in P-model is the balance between the cost of carboxylation and transpiration fluxes. The validation reported by Stocker et al. (2020) shows daily RMSE 1.96 g C m^{-2} d^{-1} (R^2 = 0.75) and annual RMSE 399 g C m^{-2} yr^{-1} (R^2 = 0.69). Although $Vcmax_{25}$ and g_s values are not required for the model run, there is at least one other parameter that has to be calibrated against the data, the intrinsic quantum yield (ϕ_0).

4.2. Ecosystem-specific cautions

This study examined SCOPE model performance across 10 PFTs and 3 climatic zones, some of which required specific model adjustments. The largest discrepancy was observed in λE for some sites in Subtropical Mediterranean climatic zone due to the seasonal drought period. Mediterranean dehesa's (or montado's) represent a complicated case for modelling, especially of energy balance fluxes. Their complexity lies in their multilayer structure: the overstorey is represented by sparsely located evergreen trees (*Quercus ilex*), whereas the understory consists of grasses and has a strong seasonal pattern, being green in the wet period (October–April) and dry (bare soil) in the drought period. Burchard-Levine et al. (2020, 2022) adapted a two-source energy balance for SAV, converting it into a three-source model. Pacheco-Labrador et al. (2019, 2021) made an effort to adapt SCOPE for Mediterranean grasses by including non-green leaves into the canopy. Modelling r_{ss} from soil moisture and using LST to constrain the energy balance are two fundamentally different approaches. In SAV (the dehesa system) the canopy is rather closed, and LST is affected by both soil and vegetation temperature, but the retrieval of two dynamic parameters (r_{ss}, BallBerrySlope) from one (LST) is ill-posed, and hence, a combination of energy and water balance constraints may be pursued.

The use of 300 m pixels is sub-optimal CRO systems, and complementary information from high resolution (10–20 m) data and crop rotation are required for correct interpretation at field scale. Our analysis showed that at 300 m the C3 parametrization performed better than the crop-dependent C3/C4 parametrization, but this may also be due to the lack of crop-specific values for $Vcmax_{25}$ and BallBerrySlope. The footprint of eddy-covariance towers depends on their height, wind speed and atmospheric stability and it typically lies within 200 m for CRO (Chu et al., 2021). For towers located on the border of the two fields (DE-Geb) or surrounded by other PFT (FI-Qvd), weighting of the half hourly flux by wind direction can lead to more precise estimates (Heimsch et al., 2021).

The validation dataset comprised a large number of forest sites (ENF, MF, DBF, EBF). The turbid-medium representation in SCOPE for radiative transfer may not suffice, due to effects of foliage clumping that are not considered as for example, in the CliMA model (Wang et al., 2021a). Although a clumping index for radiative transfer was already proposed in the soil–leaf-canopy (SLC) model (Verhoef and Bach, 2007), the influence of clumping on λE and LST via the aerodynamic resistance scheme remains unclear. Although not including clumping may lead to the underestimation of GPP (Chen et al., 2012), the flux simulations for forests in our study appeared even more accurate than for herbaceous ecosystems.

By choosing PFT dependent parameter sets, the difference within PFT's were not considered. For wetlands (WET) this approach appeared insufficient. No single set of parameters could reproduce the large difference in GPP between southern (10-12 μmol CO_2 m^{-2} s^{-1}) and northern sites (< 5 μmol CO_2 m^{-2} s^{-1}). However, fitting of $Vcmax_{25}$ and BallBerrySlope for individual sites is not meaningful if the purpose is a global application.

5. Conclusion

In this work, we evaluated SCOPE-simulated carbon and energy fluxes across 63 European eddy covariance sites of 10 plant functional types (PFT) at daily and yearly time steps. SCOPE was constrained with Sentinel-3 optical data and global reanalysis ERA5-land meteorological data. PFT-specific literature values of maximum carboxylation capacity ($Vcmax_{25}$) and BallBerrySlope were tested as an alternative to the default values. The addition of LAI seasonally to $Vcmax_{25}$ reduced the bias in flux estimations. We demonstrated the ways of water stress accounting through the computation of the soil resistance to evaporation from porous space (r_{ss}) parameter from soil moisture content (SMC) or land surface temperature (LST), which was required in drought-prone subtropical Mediterranean ecosystems. We conclude that SCOPE with PFT-specific seasonally varying $Vcmax_{25}$ and PFT-specific BallBerrySlope simulates the ecosystem GPP and ET on daily and annual scales well, but compared to the default parametrization of these parameters the improvement was modest. We acknowledge the fact that even better performance can be achieved with SCOPE calibration per dataset or per each eddy covariance site, however, the aim of this study was to evaluate the performance of SCOPE model in general, paving a way to its further application in large-scale and global mapping. The study further suggests that most improvement can be expected from including a satellite-derived constraint on water-limited fluxes in the model.

Code and data availability

SCOPE v.2.1	https://github.com/Christiaanvandertol/SCOPE docs: https://scope-model.rtfd.io
SALib	https://github.com/SALib/SALib docs: https://salib.rtfd.io
Copernicus Global Land Service LAI	https://land.copernicus.eu/global/products/lai
Warm Winter 2020 ecosystem eddy covariance flux product	https://doi.org/10.18160/2G60-ZHAK
ERA5-Land hourly data from 1981 to present	https://doi.org/10.24381/cds.e2161bac

Funding

EP, MM and CvdT has received funding from the European Union's Horizon 2020 research and innovation programme under the Marie Sklodowska-Curie grant agreement No 721995.

CRediT authorship contribution statement

Egor Prikaziuk: Software, Conceptualization, Writing – original draft, Writing – review & editing , Computation, Visualization, Data curation. **Mirco Migliavacca:** conceptualization, Writing – original draft, Resources. **Zhongbo (Bob) Su:** Writing – original draft, Writing – review & editing. **Christiaan van der Tol:** Software, Supervision, Conceptualization, Writing – original draft, Writing – review & editing, Funding acquisition.

Declaration of competing interest

The authors declare that they have no known competing financial interests or personal relationships that could have appeared to influence the work reported in this paper.

Data availability

Data will be made available on request.

Acknowledgements

The authors thank Max Planck Institute for Biogeochemistry (MPI-BGC) for computational support and the Warm Winter 2020 Task Force and the Ecosystem Thematic Centre of the ICOS Research Infrastructure for data provision. This research was supported by the Action CA17134 SENSECO (Optical synergies for spatiotemporal sensing of scalable ecophysiological traits) funded by COST (European Cooperation in Science and Technology, www.cost.eu). Data acquisition at FR-Aur and FR-Lam are mainly funded by the Institut National des Sciences de l'Univers (INSU) through the ICOS ERIC and the OSR SW observatory (https:

//osr.cesbio.cnrs.fr/). Facilities and staff are funded and supported by the Observatory Midi-Pyrenean, the University Paul Sabatier of Toulouse 3, CNRS (Centre National de la Recherche Scientifique), CNES (Centre National d'Etude Spatial) and IRD (Institut de Recherche pour le Développement). We are grateful to Franck Granouillac, Baptiste Lemaire, Nicole Claverie and Bartosz Zawilski for their technical support, advice, and valuable assistance in the field and site management, respectively. We also thank Tiphaine Tallec and Aurore Brut for the data processing. Special thanks to Mr. Andréoni (farmer) and Ecole d'Ingénieurs Purpan and farmers for accommodating the measurement devices

Appendix A. λ to Ball-Berry slope conversion

We connected the Groenendijk's model parameter λ to SCOPE Ball-Berry slope parameter m through the C_i/C_s ratio of internal leaf CO_2 concentration (C_i) to atmospheric CO_2 concentration (C_s) as:

$$m = \frac{1.6}{RH} \cdot \sqrt{\frac{\lambda \cdot C_s^2}{1.6 \cdot D \cdot (C_s - \Gamma)}}, \tag{A.1}$$

where RH is the relative humidity, D is the vapour pressure deficit at leaf surface and Γ is the compensation mole fraction of CO_2. We calculated RH from VPD and air temperature (T_a) using the Clausius–Clapeyron relationship. Γ was calculated from Γ^* as:

$$\Gamma = \frac{\Gamma^* \cdot Vcmax_{25} + R_d \cdot k'}{Vcmax_{25} - R_d}$$

$$R_d = Rdparam \cdot Vcmax_{25}$$

$$\Gamma = \frac{\Gamma^* + Rdparam \cdot k'}{1 - Rdparam},$$

where Rd is dark respiration, $Vcmax_{25}$ is the maximum carboxylation capacity or rubisco, k' is the Michaelis–Menten constant $k' = K_c \cdot (1 + O/K_o)$, and Γ^* is the compensation point in the absence of dark respiration.

We followed Groenendijk's values of $K_c = 460$ μbar, $K_o = 330$ mbar, $O = 210$ per mille, $Rdparam = 0.07$ and the following calculation of Γ^*:

$$\Gamma^* = 0.5 \cdot K_c \cdot \frac{O}{K_o} \cdot \frac{V_{om}}{V_{cm}}$$

$$\frac{V_{om}}{V_{cm}} = 0.21,$$

which led to $\Gamma^* = 3.0e^{-5}$ μbar, $\Gamma = 8.8e^{-5}$ μbar, $(C_s - \Gamma) = 3.1e^{-4}$ μbar.

Groenendijk et al. (2011) reported values the ratio of the derivatives of transpiration (E) to photosynthesis (A) to stomatal conductance (g_s) as:

$$\lambda = \frac{\partial E/\partial g_s}{\partial A/\partial g_s} \tag{A.2}$$

And the C_i/C_s ratio through λ was introduced by Lloyd and Farquhar (1994) (Eq. (11) therein):

$$\frac{C_i}{C_s} = 1 - \sqrt{\frac{1.6 \cdot D \cdot (C_s - \Gamma)}{\lambda \cdot C_s^2}}, \tag{A.3}$$

SCOPE calculates C_i/C_s using Ball-Berry m, the slope of photosynthesis-stomatal conductance line:

$$\frac{C_i}{C_s} = 1 - \frac{1.6}{m \cdot RH}, \tag{A.4}$$

where 1.6 a diffusion conversion factor.

Eq. (A.4) can be drawn from

$$g_s = m \cdot \frac{A \cdot RH}{C_s} + b, \tag{A.5}$$

where g_s — stomatal conductance, m — Ball-Berry slope, A — photosynthesis, RH — relative humidity, C_s — atmospheric CO_2 concentration, b — Ball-Berry intercept.

At equilibrium $b = 0$, $A = g_s \cdot (C_s - C_i)$ and we can substitute A in Eq. (A.5), which after some rearrangements results in Eq. (A.4).

Appendix B. Figures

B.1. ERA5 meteorological data

The ERA5 land (earlier ERA-Interim (Berrisford et al., 2011)) data disseminated within the eddy covariance flux products in FLUXNET format represent the downscaled version of the original ERA5 land dataset (Vuichard and Papale, 2015). Fig. B.12 shows the agreement between de-biased and tower-measured data, Fig. B.13 shows how non-de-biased (original) ERA5 Land data would compare to the tower-measured data. The most noticeable corrections are the adjustments of zero values of the incoming shortwave radiation (SW_IN) the altitude correction of the air pressure (PA) and the reduction of the scatter of the wind speed (WS). The latter remains the most uncertain reanalysis variable.

B.2. Effects of extinction coefficient, temperature correction and LAI-driven seasonality on $Vcmax_{25}$

See Fig. B.14.

B.3. Local sensitivity analysis of the SCOPE model

See Fig. B.15.

B.4. Site-specific results for wetlands

See Fig. B.16.

B.5. Subtropical mediterranean (drought-prone) ecosystems: LST solution

In the main matter we parametrized soil resistance to evaporation (r_{ss}) from soil moisture (Section 3.2.2) to account for λE suppression during the drought period in Subtropical Mediterranean ecosystem. Another possibility is to retrieve r_{ss} by minimizing the difference between SCOPE-simulated and satellite-observed land surface temperature (LST). LST was downloaded from the ESA CCI Sentinel-3 A (Ghent et al., 2022) and Sentinel-3B (Ghent et al., 2022) SLSTR products. This case is complicated because it requires the meteorological data at the time of the satellite overpass. Such optimization led to complete suppression of the soil λE flux (Fig. B.17).

B.6. Scenarios: Taylor plot

See Fig. B.18.

Appendix C. Tables

C.1. Warm winter 2020 sites

See Table C.5.

C.2. SCOPE parametrization

See Tables C.6 and C.7.

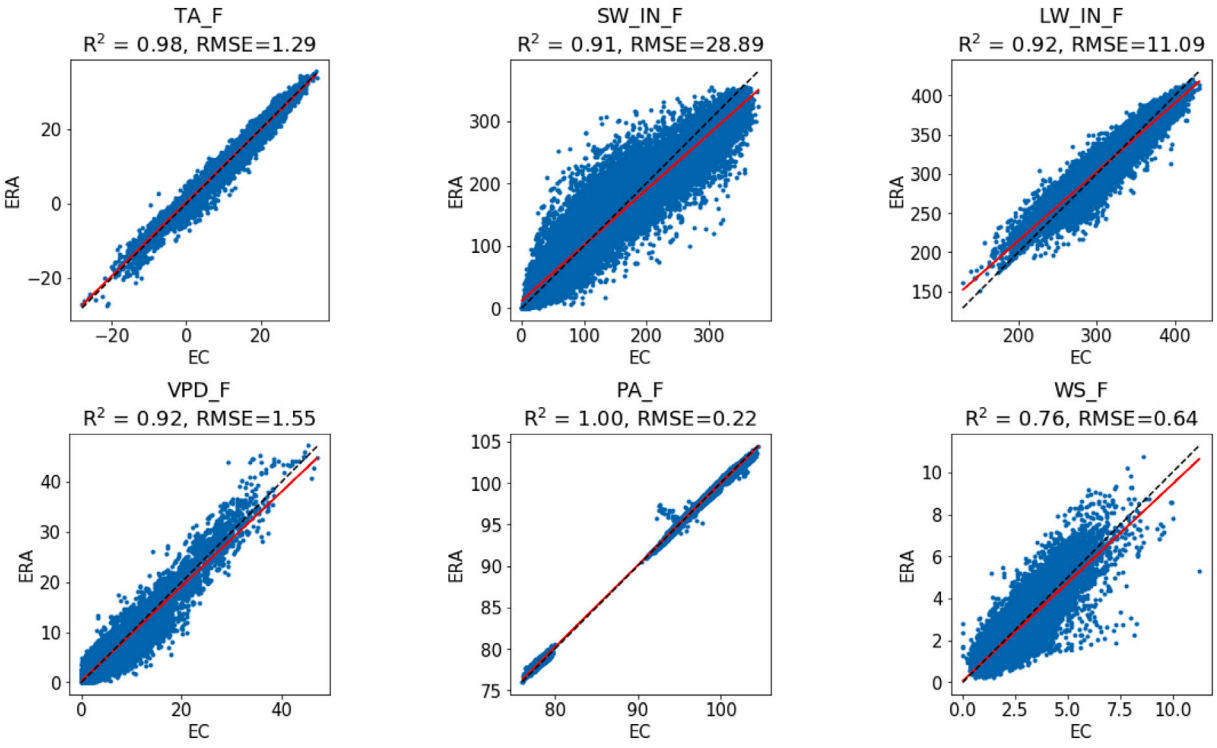

Fig. B.12. Comparison of meteorological data measured at the tower (x-axis) and de-biased ERA reanalysis data from the FLUXNET products (y-axis).

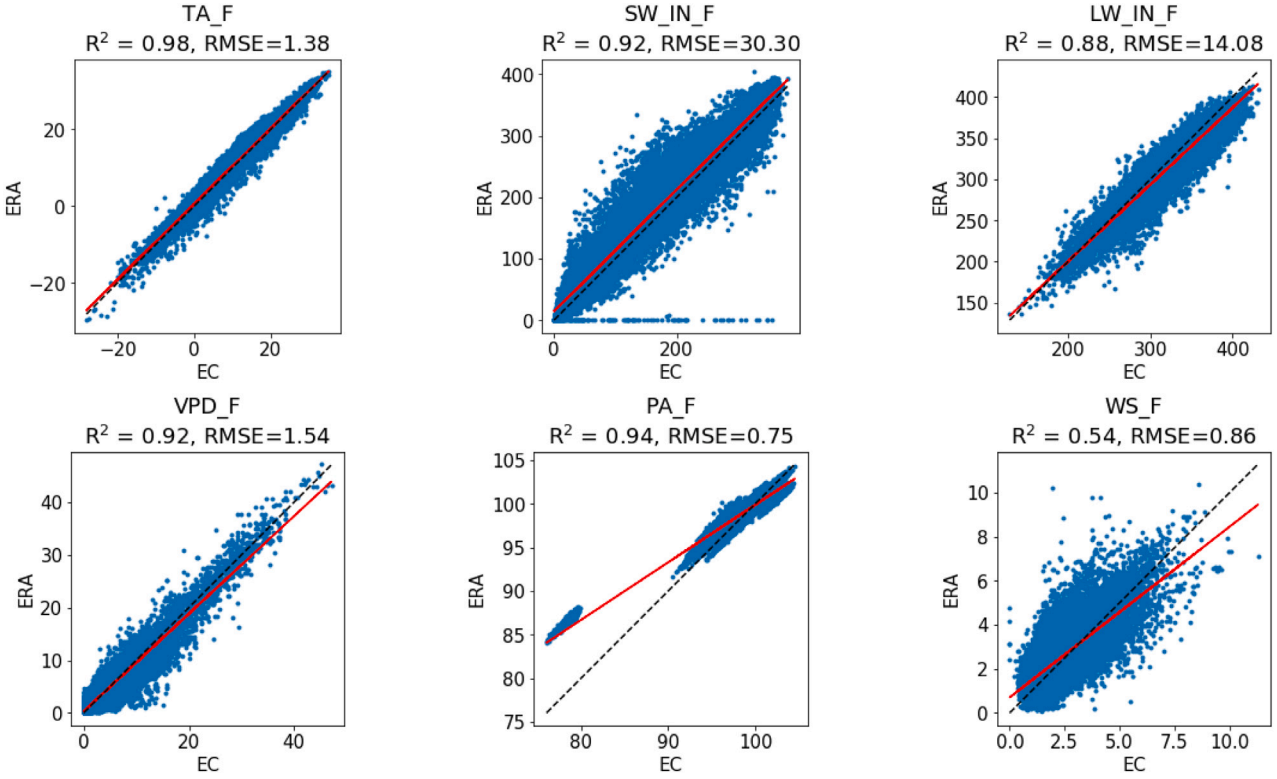

Fig. B.13. Comparison of meteorological data measured at the tower (x-axis) and extracted with the nearest neighbour method from ERA5 land data (y-axis).

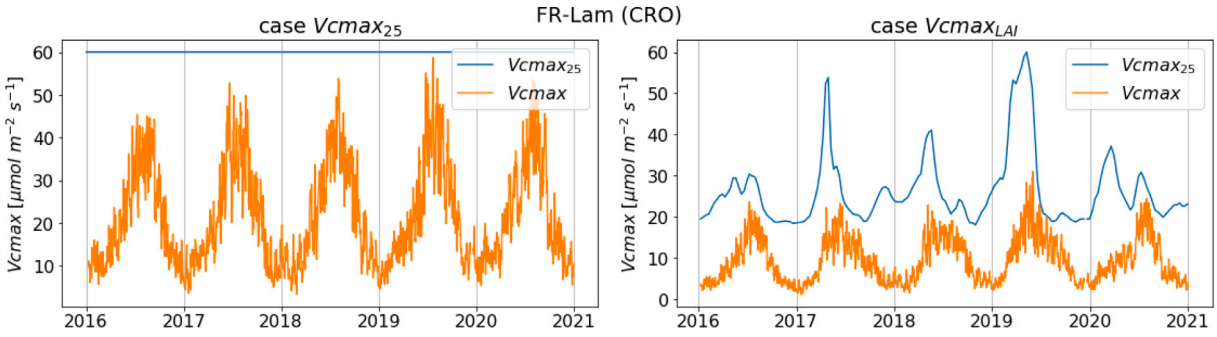

Fig. B.14. Variation of the Vcmax value between seasonally static (case $Vcmax_{25}$, left) and seasonally dynamic (case $Vcmax_{LAI}$, right) values for the case of cropland FR-Aur. Even in the static case the temperature correction lowers the input $Vcmax_{25}$ value (blue line) and creates seasonal dynamic (orange line). In SCOPE each leaf has different temperature, depending on the depth in the canopy and orientation towards the sun, therefore the temperature correction will result in different Vcmax values per leaf. In addition, the vertical extinction coefficient kV (default 0.64) lowers the mean canopy Vcmax further. Vcmax value on the graphs (orange line) represents the mean of all sunlit and shaded leaves. The $Vcmax_{LAI}$ was scaled based on LAI so that the peak value corresponds to the default value of the static case. (For interpretation of the references to colour in this figure legend, the reader is referred to the web version of this article.)

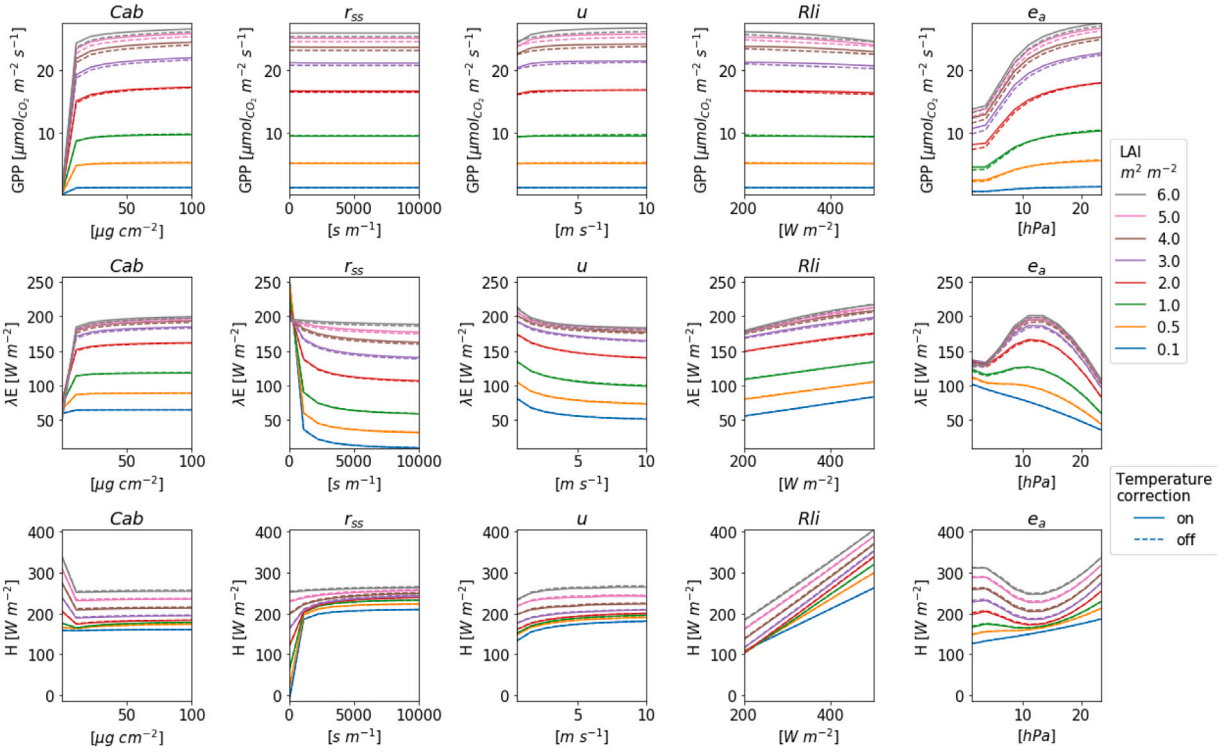

Fig. B.15. Local sensitivity analysis of SCOPE modelled fluxes at varying LAI levels (legend). Top — gross primary productivity (GPP), middle — latent heat flux (λE), bottom — sensible heat flux (H). *Cab* — leaf chlorophyll content, r_{ss} — soil resistance to evaporation, u — wind speed, *Rli* — incoming longwave radiation, e_a — atmospheric vapour pressure. Main matter Fig. 3.

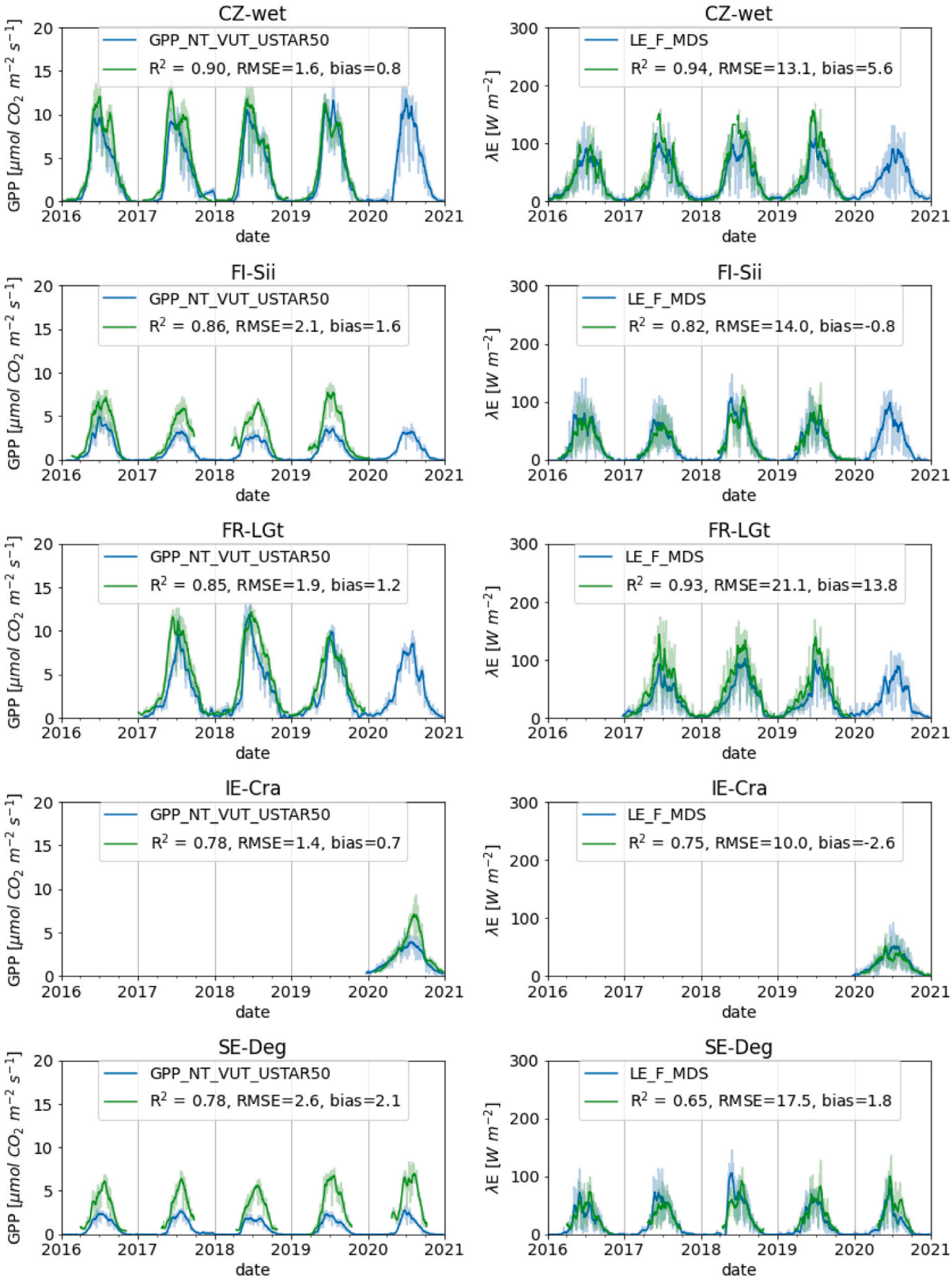

Fig. B.16. Performance of SCOPE-simulated GPP and λE for WET. Blue — measured flux, green — Groenendijk seasonal $Vcmax_{LAI}$ case. Shading — real data, line — 15-day moving average. (For interpretation of the references to colour in this figure legend, the reader is referred to the web version of this article.)

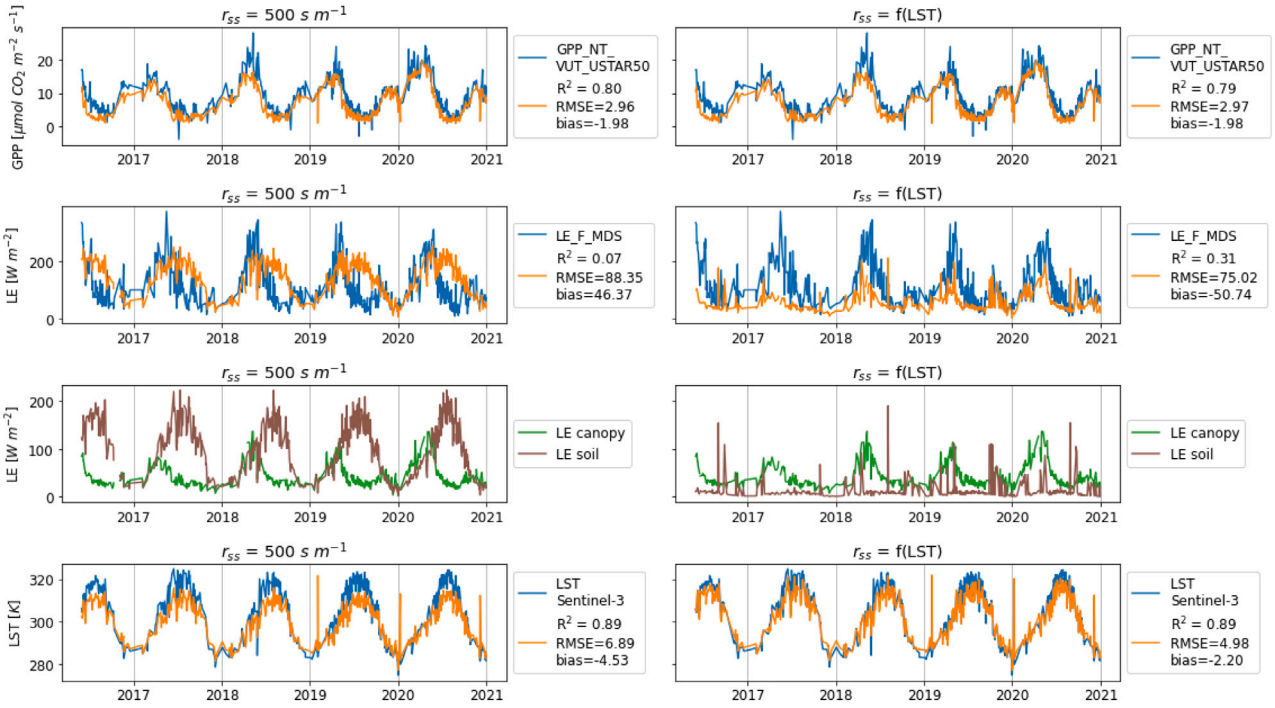

Fig. B.17. The retrieval of r_{ss} from land surface temperature (LST), the case of Mediterranean dehesas (SAV) ES-LM1 site. Notice, the measurements are presented at the overpass time (around 11:00 UTC).

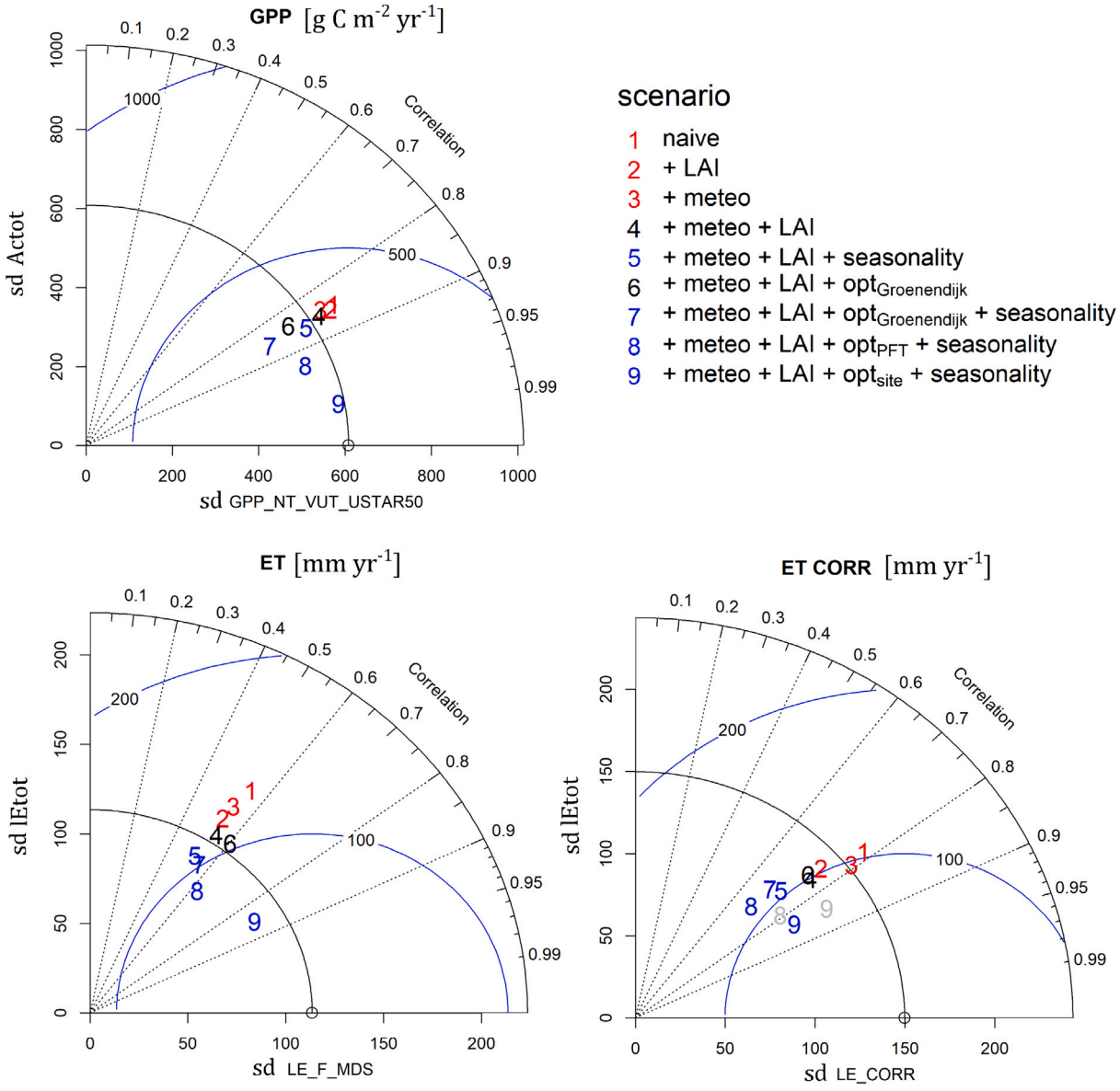

Fig. B.18. Performance of the SCOPE model in various scenarios (Table 4) for annual accumulated GPP and ET fluxes (ET CORR — measured ET flux, corrected for energy balance closure (LE_CORR), ET — measured, uncorrected, computed from LE_F_MDS). *x*-axis — standard deviation of the measured flux, *y*-axis — standard deviation of the modelled flux, dotted radial lines — correlation coefficient between modelled and measured data, blue hemispherical arches — de-biased (centred) RMSE. The best model (matching standard deviation, low centred RMSE, highest correlation coefficient) would be located at the bottom of the black hemispherical arches (close to the hollow point on the x-axis). Red points — theoretical scenarios, black — Vcmax static case ($Vcmax_{25}$), blue — Vcmax seasonal case ($Vcmax_{LAI}$), grey — scenarios optimized for ET CORR flux. Main matter Fig. 11. (For interpretation of the references to colour in this figure legend, the reader is referred to the web version of this article.)

Table C.5
Eddy covariance sites from Warm Winter 2020 eddy covariance flux product dataset (Warm Winter 2020 Team and ICOS Ecosystem Thematic Centre, 2022) participated in this study. z — measurement height [m], hc — canopy height [m], tz — time zone in relation to UTC. Climate classification: TE — temperate, TC — continental, BO — boreal, SM — subtropical Mediterranean.

PFT	site_code	lat	lon	z	hc	tz	site_years	climate
CRO	BE-Lon	4.75	50.55	2.7	1	1	5	TE
CRO	CH-Oe2	7.73	47.29	2	1	1	4	TC
CRO	CZ-KrP	15.08	49.57	10	1	1	5	TC
CRO	DE-Geb	10.91	51.1	2	1	1	4	TC
CRO	DE-Kli	13.52	50.89	2	1	1	4	TC
CRO	DE-RuS	6.45	50.87	2	1	1	5	TE
CRO	FI-Qvd	22.39	60.3	2.3	0.5	2	2	TC
CRO	FR-Aur	1.11	43.55	3.5	1	1	5	TE
CRO	FR-Lam	1.24	43.5	3.5	1.5	1	4	TE
GRA	BE-Dor	4.97	50.31	1.5	0.1	1	5	TE
GRA	CH-Aws	9.79	46.58	2	0.5	1	4	TC
GRA	CH-Cha	8.41	47.21	2	1	1	4	TC
GRA	CH-Fru	8.54	47.12	2	1	1	4	TC
GRA	DE-Gri	13.51	50.95	3	0.21	1	4	TC
GRA	DE-RuR	6.3	50.62	2	1	1	5	TC
GRA	IT-MBo	11.05	46.01	4	0.3	1	4	TC
GRA	IT-Tor	7.58	45.84	2	1	1	4	BO
ENF	CH-Dav	9.86	46.82	35	25	1	4	TC
ENF	CZ-BK1	18.54	49.5	25.5	17	1	4	TC
ENF	CZ-RAJ	16.7	49.44	25.5	17	1	4	TC
ENF	DE-Obe	13.72	50.79	25.5	17	1	4	TC
ENF	DE-RuW	6.33	50.5	25.5	17	1	5	TC
ENF	DE-Tha	13.57	50.96	26.5	18.55	1	4	TC
ENF	FI-Hyy	24.29	61.85	23.3	14	2	4	BO
ENF	FI-Ken	24.24	67.99	23	13	2	2	BO
ENF	FI-Let	23.96	60.64	25.5	20	2	5	BO
ENF	FI-Var	29.61	67.75	15	8	2	5	BO
ENF	FR-Bil	−0.96	44.49	23.3	14	1	5	TE
ENF	IL-Yat	35.05	31.35	20	10	2	5	SM
ENF	IT-Lav	11.28	45.96	42	28	1	4	TC
ENF	IT-Ren	11.43	46.59	35	25	1	5	TC
ENF	IT-SR2	10.29	43.73	23.3	14	1	5	SM
ENF	RU-Fy2	32.9	56.45	29	27.4	4	5	TC
ENF	RU-Fyo	32.92	56.46	29	27.4	4	4	TC
ENF	SE-Htm	13.42	56.1	27	19	1	5	TC
ENF	SE-Nor	17.48	60.09	36	25	1	5	TC
ENF	SE-Ros	19.74	64.17	23.3	14	1	5	BO
ENF	SE-Svb	19.77	64.26	32.5	20	1	4	BO
MF	BE-Bra	4.52	51.31	40	26	1	4	TE
MF	BE-Vie	6	50.3	52	33	1	5	TC
MF	CH-Lae	8.36	47.48	47	30.6	1	4	TC
MF	CZ-Lnz	16.95	48.68	44	27	1	4	TC
MF	FR-FBn	5.68	43.24	15	10	1	4	SM
DBF	BE-Lcr	3.85	51.11	6	4	1	1	TE
DBF	CZ-Stn	17.97	49.04	22	13	1	4	TC
DBF	DE-Hai	10.45	51.08	22	13	1	5	TC
DBF	DE-HoH	11.22	52.09	22	13	1	4	TC
DBF	DK-Sor	11.64	55.49	30	10	1	5	TC
DBF	FR-Fon	2.78	48.48	35	23	1	5	TE
DBF	FR-Hes	7.06	48.67	22	13	1	5	TE
DBF	IT-BFt	10.74	45.2	40	25	1	2	SM
EBF	ES-Cnd	−3.23	37.91	15	8	1	5	SM
SAV	ES-Abr	−6.79	38.7	15	8	1	5	SM
SAV	ES-LM1	−5.78	39.94	15	8	1	5	SM
SAV	ES-LM2	−5.78	39.93	15	8	1	5	SM
OSH	ES-LJu	−2.75	36.93	2.5	1	1	5	SM
OSH	IT-Lsn	12.75	45.74	5	2	1	5	SM
CSH	BE-Maa	5.63	50.98	4	0.7	1	4	TE
WET	CZ-wet	14.77	49.02	2	0.3	1	4	TC
WET	FI-Sii	24.19	61.83	2	0.3	2	4	BO
WET	FR-LGt	2.28	47.32	2	1	1	3	TE
WET	IE-Cra	−7.64	53.32	2	1	0	1	TE
WET	SE-Deg	19.56	64.18	1.75	0.3	1	5	BO

Table C.6
SCOPE fixed input parameters.

Parameter name	Value	Units	Meaning
Cab	40	μg cm^{-2}	leaf chlorophyll content
Cca	10	μg cm^{-2}	leaf carotenoid content
Cdm	0.012	g cm^{-2}	leaf mass per area (dry matter)
Cw	0.009	cm	equivalent leaf water thickness
Cs	0	–	senescent material (brown pigments)
$Cant$	1	μg cm^{-2}	leaf anthocyanin content
Cp	0	μg cm^{-2}	leaf protein content
Cbc	0	μg cm^{-2}	leaf brown pigment content
N	1.5	–	mesophyll structure parameter
$\rho_{thermal}$	0.01	–	leaf thermal reflectance
$\tau_{thermal}$	0.01	–	leaf thermal transmittance
BallBerry0	0.01	–	intercept of Ball-Berry equation
Type	0	–	photochemical pathway (0–C3, 1–C4)
kV	0.64	–	Vcmax canopy extinction coefficient
$Rdparam$	0	–	leaf respiration parameter
Kn_0	2.48		
Kn_α	2.83		
Kn_β	0.114		
spectrum	1	#	column number of soil spectrum used
r_{ss}	500	s m^{-1}	soil resistance to evaporation
$\rho_{s_{thermal}}$	0.06	–	soil thermal reflectance
$LIDFa$	−0.35	–	leaf inclination distribution function parameter a
$LIDFb$	−0.15	–	leaf inclination distribution function parameter b
leafwidth	0.1	m	leaf width
C_a	410	ppm	atmospheric CO_2 concentration
O_a	209	per mille	atmospheric O_2 concentration
z_0	0.25	m	canopy roughness length
d	1.34	m	displacement height
Cd	0.3	–	leaf drag coefficient
rb	10	s m^{-1}	leaf boundary resistance
CR	0.35	–	drag coefficient for isolated tree
$CD1$	20.6	–	fitting parameter
Ψ_{cor}	0.2	–	roughness layer correction
$CSSOIL$	0.01	–	drag coefficient for soil
r_{bs}	10	s m^{-1}	soil boundary layer resistance
r_{uc}	0	s m^{-1}	within canopy layer resistance
θ_o	0	°	observation zenith angle
ψ	0	°	relative azimuth angle

Table C.7
SCOPE options configuration.

State	Name	Meaning
0	lite	full SCOPE model is used
0	calc_fluor	fluorescence is not calculated
0	calc_planck	termal spectrum for each wavelength is not calculated
1	calc_xanthophyllabs	xanthophyll absorption is calculated
0	soilspectrum	soil reflectance is taken from file
0	Fluorescence_model	biochemical model of Van der Tol Berry is used
1	applTcorr	temperature correction is applied
0	verify	output is not compared
1	saveCSV	output is saved as .csv files
0	mSCOPE	mSCOPE is not used
1	simulation	time-series simulations
0	calc_directional	directional output is not computed
0	calc_vert_profiles	vertical profiles are not computed
2	soil_heat_method	ground heat flux 35% of soil net radiation [set to 0% for daily]
0	calc_rss_rbs	rss and rbs are fixed
1	MoninObukhov	Monin–Obukhov atmospheric stability correction is applied
0	save_spectral	spectral files are not saved

References

Allen, R.G., Tasumi, M., Trezza, R., 2007. Satellite-Based Energy Balance for Mapping Evapotranspiration with Internalized Calibration (METRIC)—Model. J. Irrig. Drain. Eng. 133 (4), 380–394. http://dx.doi.org/10.1061/(ASCE)0733-9437(2007)133:4(380), URL: http://ascelibrary.org/doi/10.1061/%28ASCE%290733-9437%282007%29133%3A4%28380%29.

Alton, P.B., 2017. Retrieval of seasonal Rubisco-limited photosynthetic capacity at global FLUXNET sites from hyperspectral satellite remote sensing: Impact on carbon modelling. Agricult. Forest Meteorol. 232, 74–88. http://dx.doi.org/10.1016/j.agrformet.2016.08.001.

Baldocchi, D., Chu, H., Reichstein, M., 2018. Inter-annual variability of net and gross ecosystem carbon fluxes: A review. Agricult. Forest Meteorol. 249 (November 2016), 520–533. http://dx.doi.org/10.1016/j.agrformet.2017.05.015, URL: https://linkinghub.elsevier.com/retrieve/pii/S0168192317301806.

Bastiaanssen, W., Menenti, M., Feddes, R., Holtslag, A., 1998. A remote sensing surface energy balance algorithm for land (SEBAL). 1. Formulation. J. Hydrol. 212–213, 198–212. http://dx.doi.org/10.1016/S0022-1694(98)00253-4, URL: https://linkinghub.elsevier.com/retrieve/pii/S0022169498002534.

Bayat, B., Van der Tol, C., Verhoef, W., 2018. Integrating satellite optical and thermal infrared observations for improving daily ecosystem functioning estimations during a drought episode. Remote Sens. Environ. 209 (March), 375–394. http://dx.doi.org/10.1016/j.rse.2018.02.027, URL: http://linkinghub.elsevier.com/retrieve/pii/S0034425718300336.

Bayat, B., van der Tol, C., Yang, P., Verhoef, W., 2019. Extending the SCOPE model to combine optical reflectance and soil moisture observations for remote sensing of ecosystem functioning under water stress conditions. Remote Sens.

Environ. 221, 286–301. http://dx.doi.org/10.1016/j.rse.2018.11.021, URL: https://linkinghub.elsevier.com/retrieve/pii/S0034425718305303.

Beer, C., Reichstein, M., Tomelleri, E., Ciais, P., Jung, M., Carvalhais, N., Rödenbeck, C., Arain, M.A., Baldocchi, D., Bonan, G.B., Bondeau, A., Cescatti, A., Lasslop, G., Lindroth, A., Lomas, M., Luyssaert, S., Margolis, H., Oleson, K.W., Roupsard, O., Veenendaal, E., Viovy, N., Williams, C., Woodward, F.I., Papale, D., 2010. Terrestrial gross carbon dioxide uptake: Global distribution and covariation with climate. Science 329 (5993), 834–838. http://dx.doi.org/10.1126/science.1184984, URL: https://www.sciencemag.org/lookup/doi/10.1126/science.1184984.

Bégué, A., Arvor, D., Bellon, B., Betbeder, J., de Abelleyra, D., Ferraz, R.P., Lebourgeois, V., Lelong, C., Simões, M., Verón, S.R., 2018. Remote sensing and cropping practices: A review. Remote Sens. 10 (1), 1–32. http://dx.doi.org/10.3390/rs10010099.

Berrisford, P., Dee, D., Poli, P., Brugge, R., Fielding, M., Fuentes, M., Kållberg, P., Kobayashi, S., Uppala, S., Simmons, A., 2011. The ERA-interim archive version 2.0. p. 23, URL: https://www.ecmwf.int/node/8174.

Best, M.J., Pryor, M., Clark, D.B., Rooney, G.G., Essery, R.L.H., Ménard, C.B., Edwards, J.M., Hendry, M.A., Porson, A., Gedney, N., Mercado, L.M., Sitch, S., Blyth, E., Boucher, O., Cox, P.M., Grimmond, C.S.B., Harding, R.J., 2011. The Joint UK Land Environment Simulator (JULES), model description – Part 1: Energy and water fluxes. Geosci. Model Dev. 4 (3), 677–699. http://dx.doi.org/10.5194/gmd-4-677-2011, URL: https://gmd.copernicus.org/articles/4/677/2011/.

Bezy, J.L., Delwart, S., Rast, M., 2000. MERIS — A new generation of ocean-colour sensor onboard sEnvisat. Esa Bull.-Eur. Space Agency (August 2000), 48–56.

Biriukova, K., Celesti, M., Evdokimov, A., Pacheco-Labrador, J., Julitta, T., Migliavacca, M., Giardino, C., Miglietta, F., Colombo, R., Panigada, C., Rossini, M., 2020. Effects of varying solar-view geometry and canopy structure on solar-induced chlorophyll fluorescence and PRI. Int. J. Appl. Earth Obs. Geoinf. 89 (September 2019), 102069. http://dx.doi.org/10.1016/j.jag.2020.102069, URL: https://linkinghub.elsevier.com/retrieve/pii/S030324341931027X.

Bonan, G.B., Patton, E.G., Finnigan, J.J., Baldocchi, D.D., Harman, I.N., 2021. Moving beyond the incorrect but useful paradigm: Reevaluating big-leaf and multilayer plant canopies to model biosphere-atmosphere fluxes — A review. Agricult. Forest Meteorol. 306 (July 2020), 108435. http://dx.doi.org/10.1016/j.agrformet.2021.108435, URL: https://linkinghub.elsevier.com/retrieve/pii/S0168192321001180.

Burchard-Levine, V., Nieto, H., Riaño, D., Kustas, W.P., Migliavacca, M., El-Madany, T.S., Nelson, J.A., Andreu, A., Carrara, A., Beringer, J., Baldocchi, D., Martín, M.P., 2022. A remote sensing-based three-source energy balance model to improve global estimations of evapotranspiration in semi-arid tree-grass ecosystems. Global Change Biol. 28 (4), 1493–1515. http://dx.doi.org/10.1111/gcb.16002.

Burchard-Levine, V., Nieto, H., Riaño, D., Migliavacca, M., El-Madany, T.S., Perez-Priego, O., Carrara, A., Martín, M.P., 2020. Seasonal adaptation of the thermal-based two-source energy balance model for estimating evapotranspiration in a semiarid tree-grass ecosystem. Remote Sens. 12 (6), http://dx.doi.org/10.3390/rs12060904.

CESBIO, 2022. SIE environmental information system of CESBIO. Available online: https://sie.cesbio.omp.eu/variables.php. (Accessed 11 June 2022).

Chen, J.M., Liu, J., Cihlar, J., Goulden, M.L., 1999. Daily canopy photosynthesis model through temporal and spatial scaling for remote sensing applications. 124. pp. 99–119.

Chen, J.M., Mo, G., Pisek, J., Liu, J., Deng, F., Ishizawa, M., Chan, D., 2012. Effects of foliage clumping on the estimation of global terrestrial gross primary productivity. Glob. Biogeochem. Cycles 26 (1), 1–18. http://dx.doi.org/10.1029/2010GB003996.

Chu, H., Luo, X., Ouyang, Z., Chan, W.S., Dengel, S., Biraud, S.C., Torn, M.S., Metzger, S., Kumar, J., Arain, M.A., Arkebauer, T.J., Baldocchi, D., Bernacchi, C., Billesbach, D., Black, T.A., Blanken, P.D., Bohrer, G., Bracho, R., Brown, S., Brunsell, N.A., Chen, J., Chen, X., Clark, K., Desai, A.R., Duman, T., Durden, D., Fares, S., Forbrich, I., Gamon, J.A., Gough, C.M., Griffis, T., Helbig, M., Hollinger, D., Humphreys, E., Ikawa, H., Iwata, H., Ju, Y., Knowles, J.F., Knox, S.H., Kobayashi, H., Kolb, T., Law, B., Lee, X., Litvak, M., Liu, H., Munger, J.W., Noormets, A., Novick, K., Oberbauer, S.F., Oechel, W., Oikawa, P., Papuga, S.A., Pendall, E., Prajapati, P., Prueger, J., Quinton, W.L., Richardson, A.D., Russell, E.S., Scott, R.L., Starr, G., Staebler, R., Stoy, P.C., Stuart-Haëntjens, E., Sonnentag, O., Sullivan, R.C., Suyker, A., Ueyama, M., Vargas, R., Wood, J.D., Zona, D., 2021. Representativeness of Eddy-Covariance flux footprints for areas surrounding AmeriFlux sites. Agricult. Forest Meteorol. 301–302, 108350. http://dx.doi.org/10.1016/j.agrformet.2021.108350, URL: https://linkinghub.elsevier.com/retrieve/pii/S0168192321000332.

Clark, D.B., Mercado, L.M., Sitch, S., Jones, C.D., Gedney, N., Best, M.J., Pryor, M., Rooney, G.G., Essery, R.L.H., Blyth, E., Boucher, O., Harding, R.J., Huntingford, C., Cox, P.M., 2011. The Joint UK Land Environment Simulator (JULES), model description – Part 2: Carbon fluxes and vegetation dynamics. Geosci. Model Dev. 4 (3), 701–722. http://dx.doi.org/10.5194/gmd-4-701-2011, URL: https://gmd.copernicus.org/articles/4/701/2011/.

Collatz, G., Ball, J., Grivet, C., Berry, J.A., 1991. Physiological and environmental regulation of stomatal conductance, photosynthesis and transpiration: A model that includes a laminar boundary layer. Agricult. Forest Meteorol. 54 (2–4), 107–136. http://dx.doi.org/10.1016/0168-1923(91)90002-8, URL: https://www.e-tar.lt/portal/lt/legalAct/59821410cd9f11e6a2cac7383cbb90a3, http://linkinghub.elsevier.com/retrieve/pii/0168192391900028.

Collatz, G.J., Ribas-Carbo, M., Berry, J.J.a., 1992. Coupled photosynthesis-stomatal conductance model for leaves of C4 plants. Aust. J. Plant Physiol. 19 (5), 519. http://dx.doi.org/10.1071/PP9920519, URL: http://www.publish.csiro.au/?paper=PP9920519.

Croft, H., Chen, J.M., Luo, X., Bartlett, P., Chen, B., Staebler, R.M., 2017. Leaf chlorophyll content as a proxy for leaf photosynthetic capacity. Global Change Biol. 23 (9), 3513–3524. http://dx.doi.org/10.1111/gcb.13599.

Croft, H., Chen, J.M., Wang, R., Mo, G., Luo, S., Luo, X., He, L., Gonsamo, A., Arabian, J., Zhang, Y., Simic-Milas, A., Noland, T.L., He, Y., Homolová, L., Malenovský, Z., Yi, Q., Beringer, J., Amiri, R., Hutley, L., Arellano, P., Stahl, C., Bonal, D., 2020. The global distribution of leaf chlorophyll content. Remote Sens. Environ. 236 (September 2019), http://dx.doi.org/10.1016/j.rse.2019.111479.

Dai, Y., Zeng, X., Dickinson, R.E., Baker, I., Bonan, G.B., Bosilovich, M.G., Denning, A.S., Dirmeyer, P.A., Houser, P.R., Niu, G., Oleson, K.W., Schlosser, C.A., Yang, Z.-L., 2003. The Common Land Model. Bull. Am. Meteorol. Soc. 84 (8), 1013–1024. http://dx.doi.org/10.1175/BAMS-84-8-1013, URL: https://journals.ametsoc.org/bams/article/84/8/1013/58125/The-Common-Land-Model.

Dechant, B., Ryu, Y., Kang, M., 2019. Making full use of hyperspectral data for gross primary productivity estimation with multivariate regression: Mechanistic insights from observations and process-based simulations. Remote Sens. Environ. 234, 111435. http://dx.doi.org/10.1016/j.rse.2019.111435, URL: https://linkinghub.elsevier.com/retrieve/pii/S0034425719304547.

Donlon, C., Berruti, B., Buongiorno, A., Ferreira, M.H., Féménias, P., Frerick, J., Goryl, P., Klein, U., Laur, H., Mavrocordatos, C., Nieke, J., Rebhan, H., Seitz, B., Stroede, J., Sciarra, R., 2012. The Global Monitoring for Environment and Security (GMES) Sentinel-3 mission. Remote Sens. Environ. 120, 37–57. http://dx.doi.org/10.1016/j.rse.2011.07.024, URL: http://www.sciencedirect.com/science/article/pii/S0034425712000685, https://linkinghub.elsevier.com/retrieve/pii/S0034425712000685.

Drusch, M., Del Bello, U., Carlier, S., Colin, O., Fernandez, V., Gascon, F., Hoersch, B., Isola, C., Laberinti, P., Martimort, P., Meygret, A., Spoto, F., Sy, O., Marchese, F., Bargellini, P., 2012. Sentinel-2: ESA's Optical High-Resolution Mission for GMES Operational Services. Remote Sens. Environ. 120, 25–36. http://dx.doi.org/10.1016/j.rse.2011.11.026, URL: https://linkinghub.elsevier.com/retrieve/pii/S0034425712000636.

Drusch, M., Moreno, J., Bello, U.D., Franco, R., Goulas, Y., Huth, A., Kraft, S., Middleton, E.M., Miglietta, F., Mohammed, G., Nedbal, L., Rascher, U., Schüttemeyer, D., Verhoef, W., 2017. The FLuorescence EXplorer Mission Concept—ESA's Earth Explorer 8. IEEE Trans. Geosci. Remote Sens. 55 (3), 1273–1284.

Duffour, C., Olioso, A., Demarty, J., Van der Tol, C., Lagouarde, J.P., Tol, C.V.D., Lagouarde, J.P., 2015. An evaluation of SCOPE: A tool to simulate the directional anisotropy of satellite-measured surface temperatures. Remote Sens. Environ. 158, 362–375. http://dx.doi.org/10.1016/j.rse.2014.10.019, xURL: https://linkinghub.elsevier.com/retrieve/pii/S0034425714004295.

Dutta, D., Schimel, D.S., Sun, Y., van der Tol, C., Frankenberg, C., 2019. Optimal inverse estimation of ecosystem parameters from observations of carbon and energy fluxes. BIOGEOSCIENCES 16 (1), 77–103. http://dx.doi.org/10.5194/bg-16-77-2019.

Fang, H., Jiang, C., Li, W., Wei, S., Baret, F., Chen, J.M., Garcia-Haro, J., Liang, S., Liu, R., Myneni, R.B., Pinty, B., Xiao, Z., Zhu, Z., 2013. Characterization and intercomparison of global moderate resolution leaf area index (LAI) products: Analysis of climatologies and theoretical uncertainties. J. Geophys. Res.: Biogeosci. 118 (2), 529–548. http://dx.doi.org/10.1002/jgrg.20051.

Farquhar, G.D., von Caemmerer, S., Berry, J.A., 1980. A biochemical model of photosynthetic CO2 assimilation in leaves of C3 species. Planta 149 (1), 78–90. http://dx.doi.org/10.1007/BF00386231.

Fuster, B., Sánchez-Zapero, J., Camacho, F., García-Santos, V., Verger, A., Lacaze, R., Weiss, M., Baret, F., Smets, B., 2020. Quality assessment of PROBA-V LAI, fAPAR and fCOVER collection 300 m products of copernicus global land service. Remote Sens. 12 (6), http://dx.doi.org/10.3390/rs12061017.

Gelaro, R., McCarty, W., Suárez, M.J., Todling, R., Molod, A., Takacs, L., Randles, C.A., Darmenov, A., Bosilovich, M.G., Reichle, R., Wargan, K., Coy, L., Cullather, R., Draper, C., Akella, S., Buchard, V., Conaty, A., da Silva, A.M., Gu, W., Kim, G.K., Koster, R., Lucchesi, R., Merkova, D., Nielsen, J.E., Partyka, G., Pawson, S., Putman, W., Rienecker, M., Schubert, S.D., Sienkiewicz, M., Zhao, B., 2017. The modern-era retrospective analysis for research and applications, version 2 (MERRA-2). J. Clim. 30 (14), 5419–5454. http://dx.doi.org/10.1175/JCLI-D-16-0758.1.

Ghent, C., Veal, K., Perry, M., 2022. ESA land surface temperature climate change initiative (LST_cci): Land surface temperature from SLSTR (sea and land surface temperature radiometer) on sentinel 3a, level 3 collated (L3C) global product (2018–2020), version 3.00. http://dx.doi.org/10.5285/330b7c922a37420fabb3425671d7d7c6.

Groenendijk, M., Dolman, A.J., Van der Molen, M.K., Leuning, R., Arneth, A., Delpierre, N., Gash, J.H., Lindroth, A., Richardson, A.D., Verbeeck, H., Wohlfahrt, G., 2011. Assessing parameter variability in a photosynthesis model within and between plant functional types using global Fluxnet eddy covariance data. Agricult. Forest Meteorol. 151 (1), 22–38. http://dx.doi.org/10.1016/j.agrformet.2010.08.013.

Harrison, S.P., Cramer, W., Franklin, O., Prentice, I.C., Wang, H., Brännström, Å., de Boer, H., Dieckmann, U., Joshi, J., Keenan, T.F., Lavergne, A., Manzoni, S., Mengoli, G., Morfopoulos, C., Peñuelas, J., Pietsch, S., Rebel, K.T., Ryu, Y.,

Smith, N.G., Stocker, B.D., Wright, I.J., 2021. Eco-evolutionary optimality as a means to improve vegetation and land-surface models. New Phytol. 231 (6), 2125–2141. http://dx.doi.org/10.1111/nph.17558.

He, L., Chen, J.M., Liu, J., Zheng, T., Wang, R., Joiner, J., Chou, S., Chen, B., Liu, Y., Liu, R., Rogers, C., 2019. Diverse photosynthetic capacity of global ecosystems mapped by satellite chlorophyll fluorescence measurements. Remote Sens. Environ. 232 (April), 111344. http://dx.doi.org/10.1016/j.rse.2019.111344.

Heimsch, L., Lohila, A., Tuovinen, J.P., Vekuri, H., Heinonsalo, J., Nevalainen, O., Korkiakoski, M., Liski, J., Laurila, T., Kulmala, L., 2021. Carbon dioxide fluxes and carbon balance of an agricultural grassland in southern Finland. Biogeosciences 18 (11), 3467–3483. http://dx.doi.org/10.5194/bg-18-3467-2021, URL: https://bg.copernicus.org/articles/18/3467/2021/.

Hersbach, H., Bell, B., Berrisford, P., Hirahara, S., Horányi, A., Muñoz-Sabater, J., Nicolas, J., Peubey, C., Radu, R., Schepers, D., Simmons, A., Soci, C., Abdalla, S., Abellan, X., Balsamo, G., Bechtold, P., Biavati, G., Bidlot, J., Bonavita, M., Chiara, G., Dahlgren, P., Dee, D., Diamantakis, M., Dragani, R., Flemming, J., Forbes, R., Fuentes, M., Geer, A., Haimberger, L., Healy, S., Hogan, R.J., Hólm, E., Janisková, M., Keeley, S., Laloyaux, P., Lopez, P., Lupu, C., Radnoti, G., Rosnay, P., Rozum, I., Vamborg, F., Villaume, S., Thépaut, J.N., 2020. The ERA5 global reanalysis. Q. J. R. Meteorol. Soc. 146 (730), 1999–2049. http://dx.doi.org/10.1002/qj.3803, URL: https://onlinelibrary.wiley.com/doi/abs/10.1002/qj.3803.

Homolová, L., Malenovský, Z., Clevers, J.G., García-Santos, G., Schaepman, M.E., 2013. Review of optical-based remote sensing for plant trait mapping. Ecol. Complex. 15, 1–16. http://dx.doi.org/10.1016/j.ecocom.2013.06.003, URL: http://www.geo.uzh.ch/microsite/rsl-documents/research/publications/peer-reviewed-articles/Homolova_Ecological_Complexity_15_2013-1057588992/Homolova_Ecological_Complexity_15_2013.pdf, http://linkinghub.elsevier.com/retrieve/pii/S1476945X13000524.

Houborg, R., Cescatti, A., Migliavacca, M., Kustas, W., 2013. Satellite retrievals of leaf chlorophyll and photosynthetic capacity for improved modeling of GPP. Agricult. Forest Meteorol. 177 (1), 10–23. http://dx.doi.org/10.1016/j.agrformet.2013.04.006, URL: https://linkinghub.elsevier.com/retrieve/pii/S016819231300083X.

Huntzinger, D., Post, W., Wei, Y., Michalak, A., West, T., Jacobson, A., Baker, I., Chen, J., Davis, K., Hayes, D., Hoffman, F., Jain, A., Liu, S., McGuire, A., Neilson, R., Potter, C., Poulter, B., Price, D., Raczka, B., Tian, H., Thornton, P., Tomelleri, E., Viovy, N., Xiao, J., Yuan, W., Zeng, N., Zhao, M., Cook, R., 2012. North American Carbon Program (NACP) regional interim synthesis: Terrestrial biospheric model intercomparison. Ecol. Model. 232, 144–157. http://dx.doi.org/10.1016/j.ecolmodel.2012.02.004, https://linkinghub.elsevier.com/retrieve/pii/S0304380012000725.

Jiang, C., Ryu, Y., 2016. Multi-scale evaluation of global gross primary productivity and evapotranspiration products derived from Breathing Earth System Simulator (BESS). Remote Sens. Environ. 186, 528–547. http://dx.doi.org/10.1016/j.rse.2016.08.030.

Jiang, C., Ryu, Y., Fang, H., Myneni, R., Claverie, M., Zhu, Z., 2017. Inconsistencies of interannual variability and trends in long-term satellite leaf area index products. Global Change Biol. 23 (10), 4133–4146. http://dx.doi.org/10.1111/gcb.13787.

Jiang, C., Ryu, Y., Wang, H., Keenan, T.F., 2020. An optimality-based model explains seasonal variation in C3 plant photosynthetic capacity. Global Change Biol. 26 (11), 6493–6510. http://dx.doi.org/10.1111/gcb.15276.

Jin, J., Wang, Q., Wang, J., Otieno, D., 2019. Tracing water and energy fluxes and reflectance in an arid ecosystem using the integrated model SCOPE. J. Environ. Manag. 231, 1082–1090. http://dx.doi.org/10.1016/j.jenvman.2018.10.090, URL: https://linkinghub.elsevier.com/retrieve/pii/S0301479718312301.

Jung, M., Reichstein, M., Margolis, H.A., Cescatti, A., Richardson, A.D., Arain, M.A., Arneth, A., Bernhofer, C., Bonal, D., Chen, J., Gianelle, D., Gobron, N., Kiely, G., Kutsch, W., Lasslop, G., Law, B.E., Lindroth, A., Merbold, L., Montagnani, L., Moors, E.J., Papale, D., Sottocornola, M., Vaccari, F., Williams, C., 2011. Global patterns of land-atmosphere fluxes of carbon dioxide, latent heat, and sensible heat derived from eddy covariance, satellite, and meteorological observations. J. Geophys. Res. Biogeosci. 116 (3), 1–16. http://dx.doi.org/10.1029/2010JG001566.

Jung, M., Schwalm, C., Migliavacca, M., Walther, S., Camps-Valls, G., Koirala, S., Anthoni, P., Besnard, S., Bodesheim, P., Carvalhais, N., Chevallier, F., Gans, F., Goll, D.S., Haverd, V., Köhler, P., Ichii, K., Jain, A.K., Liu, J., Lombardozzi, D., Nabel, J.E.M.S., Nelson, J.A., O'Sullivan, M., Pallandt, M., Papale, D., Peters, W., Pongratz, J., Rödenbeck, C., Sitch, S., Tramontana, G., Walker, A., Weber, U., Reichstein, M., 2020. Scaling carbon fluxes from eddy covariance sites to globe: Synthesis and evaluation of the FLUXCOM approach. Biogeosciences 17 (5), 1343–1365. http://dx.doi.org/10.5194/bg-17-1343-2020, URL: https://bg.copernicus.org/articles/17/1343/2020/.

Jung, M., Vetter, M., Herold, M., Churkina, G., Reichstein, M., Zaehle, S., Ciais, P., Viovy, N., Bondeau, A., Chen, Y., Trusilova, K., Feser, F., Heimann, M., 2007. Uncertainties of modeling gross primary productivity over Europe: A systematic study on the effects of using different drivers and terrestrial biosphere models. Glob. Biogeochem. Cycles 21 (4), 1–12. http://dx.doi.org/10.1029/2006GB002915.

Justice, C., Townshend, J., Vermote, E., Masuoka, E., Wolfe, R., Saleous, N., Roy, D., Morisette, J., 2002. An overview of MODIS Land data processing and product status. Remote Sens. Environ. 83 (1–2), 3–15. http://dx.doi.org/10.1016/S0034-4257(02)00084-6, URL: https://linkinghub.elsevier.com/retrieve/pii/S0034425702000846.

Kalnay, E., Kanamitsu, M., Kistler, R., Collins, W., Deaven, D., Gandin, L., Iredell, M., Saha, S., White, G., Woollen, J., Zhu, Y., Leetmaa, A., Reynolds, R., Chelliah, M., Ebisuzaki, W., Higgins, W., Janowiak, J., Mo, K.C., Ropelewski, C., Wang, J., Jenne, R., Joseph, D., 1996. The NCEP/NCAR 40-Year Reanalysis Project. Bull. Am. Meteorol. Soc. 77 (3), 437–471. http://dx.doi.org/10.1175/1520-0477(1996)077<0437:TNYRP>2.0.CO;2, URL: https://journals.ametsoc.org/doi/pdf/10.1175/1520-0477(1996)077%3C0437%3ATNYRP%3E2.0.CO%3B2, http://journals.ametsoc.org/doi/10.1175/1520-0477(1996.

Kattge, J., Knorr, W., Raddatz, T., Wirth, C., 2009. Quantifying photosynthetic capacity and its relationship to leaf nitrogen content for global-scale terrestrial biosphere models. Global Change Biol. 15 (4), 976–991. http://dx.doi.org/10.1111/j.1365-2486.2008.01744.x.

Koffi, E.N., Rayner, P.J., Norton, A.J., Frankenberg, C., Scholze, M., 2015. Investigating the usefulness of satellite-derived fluorescence data in inferring gross primary productivity within the carbon cycle data assimilation system. Biogeosciences 12 (13), 4067–4084. http://dx.doi.org/10.5194/bg-12-4067-2015, URL: https://bg.copernicus.org/articles/12/4067/2015/.

Krinner, G., Viovy, N., de Noblet-Ducoudré, N., Ogée, J., Polcher, J., Friedlingstein, P., Ciais, P., Sitch, S., Prentice, I.C., 2005. A dynamic global vegetation model for studies of the coupled atmosphere-biosphere system. Glob. Biogeochem. Cycles 19 (1), 1–33. http://dx.doi.org/10.1029/2003GB002199, URL: http://doi.wiley.com/10.1029/2003GB002199.

Kustas, W.P., Norman, J.M., 1999. Evaluation of soil and vegetation heat flux predictions using a simple two-source model with radiometric temperatures for partial canopy cover. Agricult. Forest Meteorol. 94 (1), 13–29. http://dx.doi.org/10.1016/S0168-1923(99)00005-2, URL: https://linkinghub.elsevier.com/retrieve/pii/S0168192399000052.

Li, X., Xiao, J., 2019. Mapping photosynthesis solely from solar-induced chlorophyll fluorescence: A global, fine-resolution dataset of gross primary production derived from OCO-2. Remote Sens. 11 (21), http://dx.doi.org/10.3390/rs11212563.

Liu, L., Liu, X., Wang, Z., Zhang, B., 2015. Measurement and analysis of bidirectional SIF emissions in wheat canopies. IEEE Trans. Geosci. Remote Sens. 54 (5), 2640–2651.

Liu, Y., Xiao, J., Ju, W., Zhu, G., Wu, X., Fan, W., Li, D., Zhou, Y., 2018. Satellite-derived LAI products exhibit large discrepancies and can lead to substantial uncertainty in simulated carbon and water fluxes. Remote Sens. Environ. 206 (January 2017), 174–188. http://dx.doi.org/10.1016/j.rse.2017.12.024.

Lloyd, J., Farquhar, G.D., 1994. 13C discrimination during CO2 assimilation by the terrestrial biosphere. Oecologia 99 (3–4), 201–215. http://dx.doi.org/10.1007/BF00627732.

Luo, X., Croft, H., Chen, J.M., Bartlett, P., Staebler, R., Froelich, N., 2018. Incorporating leaf chlorophyll content into a two-leaf terrestrial biosphere model for estimating carbon and water fluxes at a forest site. Agricult. Forest Meteorol. 248 (September 2017), 156–168. http://dx.doi.org/10.1016/j.agrformet.2017.09.012.

Luo, X., Croft, H., Chen, J.M., He, L., Keenan, T.F., 2019. Improved estimates of global terrestrial photosynthesis using information on leaf chlorophyll content. Global Change Biol. 25 (7), 2499–2514. http://dx.doi.org/10.1111/gcb.14624.

Maes, W.H., Pagán, B.R., Martens, B., Gentine, P., Guanter, L., Steppe, K., Verhoest, N.E., Dorigo, W., Li, X., Xiao, J., Miralles, D.G., 2020. Sun-induced fluorescence closely linked to ecosystem transpiration as evidenced by satellite data and radiative transfer models. Remote Sens. Environ. 249 (July), 112030. http://dx.doi.org/10.1016/j.rse.2020.112030, URL: https://linkinghub.elsevier.com/retrieve/pii/S0034425720304004.

Mauder, M., Foken, T., Cuxart, J., 2020. Surface-Energy-Balance Closure over Land: A Review. Bound.-Lay. Meteorol. (0123456789), http://dx.doi.org/10.1007/s10546-020-00529-6, URL: http://link.springer.com/10.1007/s10546-020-00529-6.

Migliavacca, M., Perez-Priego, O., Rossini, M., El-Madany, T.S., Moreno, G., van der Tol, C., Rascher, U., Berninger, A., Bessenbacher, V., Burkart, A., Carrara, A., Fava, F., Guan, J.H., Hammer, T.W., Henkel, K., Juarez-Alcalde, E., Julitta, T., Kolle, O., Mart?n, M.P., Musavi, T., Pacheco-Labrador, J., P?rez-Burgue?o, A., Wutzler, T., Zaehle, S., Reichstein, M., 2017. Plant functional traits and canopy structure control the relationship between photosynthetic CO2 uptake and far-red sun-induced fluorescence in a Mediterranean grassland under different nutrient availability. New Phytol. 214 (3), 1078–1091. http://dx.doi.org/10.1111/nph.14437, URL: http://doi.wiley.com/10.1111/nph.14437.

Mohammed, G.H., Colombo, R., Middleton, E.M., Rascher, U., van der Tol, C., Nedbal, L., Goulas, Y., Pérez Priego, O., Damm, A., Meroni, M., Joiner, J., Cogliati, S., Verhoef, W., Malenovský, Z., Gastellu Etchegorry, J.P., Miller, J.R., Guanter, L., Moreno, J., Moya, I., Berry, J.A., Frankenberg, C., Zarco Tejada, P.J., 2019. Remote sensing of solar-induced chlorophyll fluorescence (SIF) in vegetation: 50 years of progress. Remote Sens. Environ. 231 (October 2018), 111177. http://dx.doi.org/10.1016/j.rse.2019.04.030, URL: https://linkinghub.elsevier.com/retrieve/pii/S0034425719301816.

Monteith, J.L., 1972. Solar Radiation and Productivity in Tropical Ecosystems. J. Appl. Ecol. 9 (3), 747. http://dx.doi.org/10.2307/2401901, URL: https://www.jstor.org/stable/2401901?origin=crossref.

Muñoz Sabater, J., 2019. ERA5-land hourly data from 1981 to present. Copernicus climate change service (C3S) climate data store (CDS). http://dx.doi.org/10.24381/cds.e2161bac, Available online: (Accessed 3 March 2021).

Norman, J.M., 1979. Modeling the complete crop canopy. In: Modification of the Aerial Environment of Plants, vol. 2, pp. 249–277, URL: https://ci.nii.ac.jp/naid/10012299681.

Norman, J.M., Kustas, W.P., Humes, K.S., 1995. Source approach for estimating soil and vegetation energy fluxes in observations of directional radiometric surface temperature. Agricult. Forest Meteorol. 77 (3–4), 263–293. http://dx.doi.org/10.1016/0168-1923(95)02265-Y.

Norton, A.J., Rayner, P.J., Koffi, E.N., Scholze, M., Silver, J.D., Wang, Y.P., 2019. Estimating global gross primary productivity using chlorophyll fluorescence and a data assimilation system with the BETHY-SCOPE model. BIOGEOSCIENCES 16 (15), 3069–3093. http://dx.doi.org/10.5194/bg-16-3069-2019.

Pacheco-Labrador, J., El-Madany, T.S., van der Tol, C., Martin, M.P., Gonzalez-Cascon, R., Perez-Priego, O., Guan, J., Moreno, G., Carrara, A., Reichstein, M., Migliavacca, M., 2021. senSCOPE: Modeling mixed canopies combining green and brown senesced leaves. Evaluation in a Mediterranean Grassland. Remote Sens. Environ. 257, 112352. http://dx.doi.org/10.1016/j.rse.2021.112352, URL: https://linkinghub.elsevier.com/retrieve/pii/S0034425721000705.

Pacheco-Labrador, J., Perez-Priego, O., El-Madany, T.S., Julitta, T., Rossini, M., Guan, J., Moreno, G., Carvalhais, N., Martín, M.P., Gonzalez-Cascon, R., Kolle, O., Reischtein, M., Van der Tol, C., Carrara, A., Martini, D., Hammer, T.W., Moossen, H., Migliavacca, M., 2019. Multiple-constraint inversion of SCOPE. Evaluating the potential of GPP and SIF for the retrieval of plant functional traits. Remote Sens. Environ. 234 (October), 111362. http://dx.doi.org/10.1016/j.rse.2019.111362, URL: https://linkinghub.elsevier.com/retrieve/pii/S0034425719303815.

Pardo, N., Sánchez, M.L., Su, Z., Pérez, I.A., García, M.A., 2018. SCOPE model applied for rapeseed in Spain. Sci. Total Environ. 627, 417–426. http://dx.doi.org/10.1016/j.scitotenv.2018.01.247, https://linkinghub.elsevier.com/retrieve/pii/S0048969718302894.

Pastor-Guzman, J., Brown, L., Morris, H., Bourg, L., Goryl, P., Dransfeld, S., Dash, J., 2020. The Sentinel-3 OLCI Terrestrial Chlorophyll Index (OTCI): Algorithm Improvements, Spatiotemporal Consistency and Continuity with the MERIS Archive. Remote Sens. 12 (16), 2652. http://dx.doi.org/10.3390/rs12162652, URL: https://www.mdpi.com/2072-4292/12/16/2652.

Pastorello, G., Trotta, C., Canfora, E., Chu, H., Christianson, D., Cheah, Y.W., Poindexter, C., Chen, J., Elbashandy, A., Humphrey, M., Isaac, P., Polidori, D., Ribeca, A., van Ingen, C., Zhang, L., Amiro, B., Ammann, C., Arain, M.A., Ardö, J., Arkebauer, T., Arndt, S.K., Arriga, N., Aubinet, M., Aurela, M., Baldocchi, D., Barr, A., Beamesderfer, E., Marchesini, L.B., Bergeron, O., Beringer, J., Bernhofer, C., Berveiller, D., Billesbach, D., Black, T.A., Blanken, P.D., Bohrer, G., Boike, J., Bolstad, P.V., Bonal, D., Bonnefond, J.M., Bowling, D.R., Bracho, R., Brodeur, J., Brümmer, C., Buchmann, N., Burban, B., Burns, S.P., Buysse, P., Cale, P., Cavagna, M., Cellier, P., Chen, S., Chini, I., Christensen, T.R., Cleverly, J., Collalti, A., Consalvo, C., Cook, B.D., Cook, D., Coursolle, C., Cremonese, E., Curtis, P.S., D'Andrea, E., da Rocha, H., Dai, X., Davis, K.J., De Cinti, B., de Grandcourt, A., De Ligne, A., De Oliveira, R.C., Delpierre, N., Desai, A.R., Di Bella, C.M., di Tommasi, P., Dolman, H., Domingo, F., Dong, G., Dore, S., Duce, P., Dufrêne, E., Dunn, A., Dušek, J., Eamus, D., Eichelmann, U., ElKhidir, H.A.M., Eugster, W., Ewenz, C.M., Ewers, B., Famulari, D., Fares, S., Feigenwinter, I., Feitz, A., Fensholt, R., Filippa, G., Fischer, M., Frank, J., Galvagno, M., Gharun, M., Gianelle, D., Gielen, B., Gioli, B., Gitelson, A., Goded, I., Goeckede, M., Goldstein, A.H., Gough, C.M., Goulden, M.L., Graf, A., Griebel, A., Gruening, C., Grünwald, T., Hammerle, A., Han, S., Han, X., Hansen, B.U., Hanson, C., Hatakka, J., He, Y., Hehn, M., Heinesch, B., Hinko-Najera, N., Hörtnagl, L., Hutley, L., Ibrom, A., Ikawa, H., Jackowicz-Korczynski, M., Janouš, D., Jans, W., Jassal, R., Jiang, S., Kato, T., Khomik, M., Klatt, J., Knohl, A., Knox, S., Kobayashi, H., Koerber, G., Kolle, O., Kosugi, Y., Kotani, A., Kowalski, A., Kruijt, B., Kurbatova, J., Kutsch, W.L., Kwon, H., Launiainen, S., Laurila, T., Law, B., Leuning, R., Li, Y., Liddell, M., Limousin, J.M., Lion, M., Liska, A.J., Lohila, A., López-Ballesteros, A., López-Blanco, E., Loubet, B., Loustau, D., Lucas-Moffat, A., Lüers, J., Ma, S., Macfarlane, C., Magliulo, V., Maier, R., Mammarella, I., Manca, G., Marcolla, B., Margolis, H.A., Marras, S., Massman, W., Mastepanov, M., Matamala, R., Matthes, J.H., Mazzenga, F., McCaughey, H., McHugh, I., McMillan, A.M., Merbold, L., Meyer, W., Meyers, T., Miller, S.D., Minerbi, S., Moderow, U., Monson, R.K., Montagnani, L., Moore, C.E., Moors, E., Moreaux, V., Moureaux, C., Munger, J.W., Nakai, T., Neirynck, J., Nesic, Z., Nicolini, G., Noormets, A., Northwood, M., Nosetto, M., Nouvellon, Y., Novick, K., Oechel, W., Olesen, J.E., Ourcival, J.M., Papuga, S.A., Parmentier, F.J., Paul-Limoges, E., Pavelka, M., Peichl, M., Pendall, E., Phillips, R.P., Pilegaard, K., Pirk, N., Posse, G., Powell, T., Prasse, H., Prober, S.M., Rambal, S., Rannik, Ü., Raz-Yaseef, N., Reed, D., de Dios, V.R., Restrepo-Coupe, N., Reverter, B.R., Roland, M., Sabbatini, S., Sachs, T., Saleska, S.R., Sánchez-Cañete, E.P., Sanchez-Mejia, Z.M., Schmid, H.P., Schmidt, M., Schneider, K., Schrader, F., Schroder, I., Scott, R.L., Sedlák, P., Serrano-Ortíz, P., Shao, C., Shi, P., Shironya, I., Siebicke, L., Šigut, L., Silberstein, R., Sirca, C., Spano, D., Steinbrecher, R., Stevens, R.M., Sturtevant, C., Suyker, A., Tagesson, T., Takanashi, S., Tang, Y., Tapper, N., Thom, J., Tiedemann, F., Tomassucci, M., Tuovinen, J.P., Urbanski, S., Valentini, R., van der Molen, M., van Gorsel, E., van Huissteden, K., Varlagin, A., Verfaillie, J., Vesala, T., Vincke, C., Vitale, D., Vygodskaya, N., Walker, J.P., Walter-Shea, E., Wang, H., Weber, R., Westermann, S., Wille, C., Wofsy, S., Wohlfahrt, G., Wolf, S., Woodgate, W., Li, Y., Zampedri, R., Zhang, J., Zhou, G., Zona, D., Agarwal, D., Biraud, S., Torn, M., Papale, D., 2020. The FLUXNET2015 dataset and the ONEFlux processing pipeline for eddy covariance data. Sci. Data 7 (1), 225. http://dx.doi.org/10.1038/s41597-020-0534-3.

Paulson, C.A., 1970. The Mathematical Representation of Wind Speed and Temperature Profiles in the Unstable Atmospheric Surface Layer. J. Appl. Meteorol. 9 (6), 857–861. http://dx.doi.org/10.1175/1520-0450(1970)009<0857:TMROWS>2.0.CO;2, URL: http://journals.ametsoc.org/doi/abs/10.1175/1520-0450{%}281970{%}29009{%}3C0857{%}3ATMROWS{%}3E2.0.CO{%}3B2.

Prentice, I.C., Dong, N., Gleason, S.M., Maire, V., Wright, I.J., 2014. Balancing the costs of carbon gain and water transport: Testing a new theoretical framework for plant functional ecology. In: Penuelas, J. (Ed.), Ecol. Lett. 17 (1), 82–91. http://dx.doi.org/10.1111/ele.12211, URL: https://onlinelibrary.wiley.com/doi/10.1111/ele.12211.

Prikaziuk, E., Van der Tol, C., 2019. Global Sensitivity Analysis of the SCOPE Model in Sentinel-3 Bands: Thermal Domain Focus. Remote Sens. 11 (20), 2424. http://dx.doi.org/10.3390/rs11202424, URL: https://www.mdpi.com/2072-4292/11/20/2424.

Prikaziuk, E., Yang, P., van der Tol, C., 2021. Google EarthEngine Sentinel-3 OLCI Level-1 Dataset Deviates from the Original Data: Causes and Consequences. Remote Sens. 13 (6), 1098. http://dx.doi.org/10.3390/rs13061098, URL: https://www.mdpi.com/2072-4292/13/6/1098.

Running, S.W., Mu, Q., 2019. User ' s Guide NASA Earth Observing System MODIS Land Algorithm (For Collection 6).

Running, S.W., Mu, Q., Zhao, M., Moreno, A., 2019. MOD16A3GF MODIS/Terra Net Evapotranspiration Gap-Filled Yearly L4 Global 500 m SIN Grid V006. NASA EOSDIS Land Process. DAAC 1–37. http://dx.doi.org/10.5067/MODIS/MOD16A3GF.006.

Ryu, Y., Baldocchi, D.D., Kobayashi, H., Van Ingen, C., Li, J., Black, T.A., Beringer, J., Van Gorsel, E., Knohl, A., Law, B.E., Roupsard, O., 2011. Integration of MODIS land and atmosphere products with a coupled-process model to estimate gross primary productivity and evapotranspiration from 1 km to global scales. Glob. Biogeochem. Cycles 25 (4), 1–24. http://dx.doi.org/10.1029/2011GB004053.

Ryu, Y., Berry, J.A., Baldocchi, D.D., 2019. What is global photosynthesis? History, uncertainties and opportunities. Remote Sens. Environ. 223 (January), 95–114. http://dx.doi.org/10.1016/j.rse.2019.01.016.

Sellers, P.J., Mintz, Y., Sud, Y.C., Dalcher, A., 1986. A Simple Biosphere Model (SIB) for Use within General Circulation Models. J. Atmos. Sci. 43 (6), 505–531. http://dx.doi.org/10.1175/1520-0469(1986)043<0505:ASBMFU>2.0.CO;2, URL: http://journals.ametsoc.org/doi/10.1175/1520-0469(1986)043%3C0505:ASBMFU%3E2.0.CO;2.

Smith, N.G., Keenan, T.F., Colin Prentice, I., Wang, H., Wright, I.J., Niinemets, Ü., Crous, K.Y., Domingues, T.F., Guerrieri, R., Yoko Ishida, F., Kattge, J., Kruger, E.L., Maire, V., Rogers, A., Serbin, S.P., Tarvainen, L., Togashi, H.F., Townsend, P.A., Wang, M., Weerasinghe, L.K., Zhou, S.X., 2019. Global photosynthetic capacity is optimized to the environment. Ecol. Lett. 22 (3), 506–517. http://dx.doi.org/10.1111/ele.13210.

Stocker, B.D., Wang, H., Smith, N.G., Harrison, S.P., Keenan, T.F., Sandoval, D., Davis, T., Prentice, I.C., 2020. P-model v1.0: An optimality-based light use efficiency model for simulating ecosystem gross primary production. Geosci. Model Dev. 13 (3), 1545–1581. http://dx.doi.org/10.5194/GMD-13-1545-2020.

Su, Z., 2002. The Surface Energy Balance System (SEBS) for estimation of turbulent heat fluxes. Hydrol. Earth Syst. Sci. 6 (1), 85–100. http://dx.doi.org/10.5194/hess-6-85-2002, URL: https://hess.copernicus.org/articles/6/85/2002/.

Tian, F., Cai, Z., Jin, H., Hufkens, K., Scheifinger, H., Tagesson, T., Smets, B., Van Hoolst, R., Bonte, K., Ivits, E., Tong, X., Ardö, J., Eklundh, L., 2021. Calibrating vegetation phenology from Sentinel-2 using eddy covariance, PhenoCam, and PEP725 networks across Europe. Remote Sens. Environ. 260, 112456. http://dx.doi.org/10.1016/j.rse.2021.112456, URL: https://linkinghub.elsevier.com/retrieve/pii/S0034425721001747.

Timmermans, J., Su, Z., van der Tol, C., Verhoef, A., Verhoef, W., 2013. Quantifying the uncertainty in estimates of surface–atmosphere fluxes through joint evaluation of the SEBS and SCOPE models. Hydrol. Earth Syst. Sci. 17 (4), 1561–1573. http://dx.doi.org/10.5194/hess-17-1561-2013, URL: https://hess.copernicus.org/articles/17/1561/2013/.

Van de Griend, A.A., Owe, M., 1994. Bare soil surface resistance to evaporation by vapor diffusion under semiarid conditions. Water Resour. Res. 30 (2), 181–188. http://dx.doi.org/10.1029/93WR02747.

Van der Tol, C., Berry, J.A., Campbell, P.K.E., Rascher, U., 2014. Models of fluorescence and photosynthesis for interpreting measurements of solar-induced chlorophyll fluorescence. J. Geophys. Res.: Biogeosci. 119 (12), 2312–2327.

Van der Tol, C., Verhoef, W., Timmermans, J., Verhoef, A., Su, Z., 2009. An integrated model of soil-canopy spectral radiances, photosynthesis, fluorescence, temperature and energy balance. Biogeosciences 6 (12), 3109–3129. http://dx.doi.org/10.5194/bg-6-3109-2009, URL: www.biogeosciences.net/6/3109/2009/.

Verhoef, W., Bach, H., 2007. Coupled soil–leaf-canopy and atmosphere radiative transfer modeling to simulate hyperspectral multi-angular surface reflectance and TOA radiance data. Remote Sens. Environ. 109 (2), 166–182. http://dx.doi.org/10.1016/j.rse.2006.12.013, URL: https://linkinghub.elsevier.com/retrieve/pii/S0034425707000077.

Verhoef, A., Wallace, J., 2000. Modelling interactions in mixed-plant communities: Light, water and carbon dioxide. In: Leaf Dev. Canopy Growth, (January 2000), pp. 204–250.

Verrelst, J., Malenovský, Z., Van der Tol, C., Camps-Valls, G., Gastellu-Etchegorry, J.P., Lewis, P., North, P., Moreno, J., 2018. Quantifying Vegetation Biophysical Variables from Imaging Spectroscopy Data: A Review on Retrieval Methods. Surv. Geophys. 1–41. http://dx.doi.org/10.1007/s10712-018-9478-y.

Verrelst, J., Rivera, J.P., van der Tol, C., Magnani, F., Mohammed, G., Moreno, J., 2015. Global sensitivity analysis of the SCOPE model: What drives simulated canopy-leaving sun-induced fluorescence? Remote Sens. Environ. 166, 8–21. http://dx.doi.org/10.1016/j.rse.2015.06.002, URL: https://www.sciencedirect.com/science/article/pii/S0034425715300328.

Verrelst, J., van der Tol, C., Magnani, F., Sabater, N., Rivera, J.P., Mohammed, G., Moreno, J., 2016. Evaluating the predictive power of sun-induced chlorophyll fluorescence to estimate net photosynthesis of vegetation canopies: A SCOPE modeling study. In: Remote Sens. Environ., vol. 176, Elsevier Inc., pp. 139–151. http://dx.doi.org/10.1016/j.rse.2016.01.018.

Verseghy, D.L., 2000. The Canadian land surface scheme (CLASS): Its history and future. Atmos.-Ocean 38 (1), 1–13. http://dx.doi.org/10.1080/07055900.2000.9649637, URL: http://www.tandfonline.com/doi/abs/10.1080/07055900.2000.9649637.

VITO, 2022. Terrascope. VITO — Remote sensing. Available online: https://notebooks.terrascope.be/. (Accessed 8 October 2022).

Vuichard, N., Papale, D., 2015. Filling the gaps in meteorological continuous data measured at FLUXNET sites with ERA-Interim reanalysis. Earth Syst. Sci. Data 7 (2), 157–171. http://dx.doi.org/10.5194/essd-7-157-2015, URL: https://essd.copernicus.org/articles/7/157/2015/.

Walker, A.P., Quaife, T., van Bodegom, P.M., De Kauwe, M.G., Keenan, T.F., Joiner, J., Lomas, M.R., MacBean, N., Xu, C., Yang, X., Woodward, F.I., 2017. The impact of alternative trait-scaling hypotheses for the maximum photosynthetic carboxylation rate (Vcmax) on global gross primary production. New Phytol. 215 (4), 1370–1386. http://dx.doi.org/10.1111/nph.14623.

Wallace, J., Verhoef, A., 2000. Modelling interactions in mixed-plant communties: Light, water and carbon dioxide. Leaf Dev. Canopy Growth (May), 204–250.

Wang, R., Chen, J.M., Luo, X., Black, A., Arain, A., 2019. Seasonality of leaf area index and photosynthetic capacity for better estimation of carbon and water fluxes in evergreen conifer forests. Agricult. Forest Meteorol. 279 (August), 107708. http://dx.doi.org/10.1016/j.agrformet.2019.107708.

Wang, Y., Köhler, P., He, L., Doughty, R., Braghiere, R.K., Wood, J.D., Frankenberg, C., 2021a. Testing stomatal models at the stand level in deciduous angiosperm and evergreen gymnosperm forests using CliMA Land (v0.1). Geosci. Model Dev. 14 (11), 6741–6763. http://dx.doi.org/10.5194/gmd-14-6741-2021.

Wang, Y., Zeng, Y., Yu, L., Yang, P., Van der Tol, C., Yu, Q., Lü, X., Cai, H., Su, Z., 2021b. Integrated modeling of canopy photosynthesis, fluorescence, and the transfer of energy, mass, and momentum in the soil–plant–atmosphere continuum (STEMMUS–SCOPE v1.0.0). Geosci. Model Dev. 14 (3), 1379–1407. http://dx.doi.org/10.5194/gmd-14-1379-2021, URL: https://gmd.copernicus.org/articles/14/1379/2021/.

Warm Winter 2020 Team, ICOS Ecosystem Thematic Centre, 2022. Warm winter 2020 ecosystem eddy covariance flux product for 73 stations in FLUXNET-archive format—release 2022-1 (Version 1.0). http://dx.doi.org/10.18160/2G60-ZHAK, Available online: (Accessed 14 June 2022).

Wilson, K., Goldstein, A., Falge, E., Aubinet, M., Baldocchi, D., Berbigier, P., Bernhofer, C., Ceulemans, R., Dolman, H., Field, C., Grelle, A., Ibrom, A., Law, B., Kowalski, A., Meyers, T., Moncrieff, J., Monson, R., Oechel, W., Tenhunen, J., Valentini, R., Verma, S., 2002. Energy balance closure at FLUXNET sites. Agricult. Forest Meteorol. 113 (1–4), 223–243. http://dx.doi.org/10.1016/S0168-1923(02)00109-0, URL: http://www.sciencedirect.com/science/article/pii/S0168192302001090 https://linkinghub.elsevier.com/retrieve/pii/S0168192302001090.

Wolanin, A., Camps-Valls, G., Gómez-Chova, L., Mateo-García, G., Van der Tol, C., Zhang, Y., Guanter, L., 2019. Estimating crop primary productivity with Sentinel-2 and Landsat 8 using machine learning methods trained with radiative transfer simulations. Remote Sens. Environ. 225, 441–457. http://dx.doi.org/10.1016/j.rse.2019.03.002, URL: https://www.sciencedirect.com/science/article/pii/S0034425719300938{#}t0005, https://linkinghub.elsevier.com/retrieve/pii/S0034425719300938.

Wu, Z., Ahlström, A., Smith, B., Ardö, J., Eklundh, L., Fensholt, R., Lehsten, V., 2017. Climate data induced uncertainty in model-based estimations of terrestrial primary productivity. Environ. Res. Lett. 12 (6), http://dx.doi.org/10.1088/1748-9326/aa6fd8.

Wulder, M.A., Loveland, T.R., Roy, D.P., Crawford, C.J., Masek, J.G., Woodcock, C.E., Allen, R.G., Anderson, M.C., Belward, A.S., Cohen, W.B., Dwyer, J., Erb, A., Gao, F., Griffiths, P., Helder, D., Hermosilla, T., Hipple, J.D., Hostert, P., Hughes, M.J., Huntington, J., Johnson, D.M., Kennedy, R., Kilic, A., Li, Z., Lymburner, L., McCorkel, J., Pahlevan, N., Scambos, T.A., Schaaf, C., Schott, J.R., Sheng, Y., Storey, J., Vermote, E., Vogelmann, J., White, J.C., Wynne, R.H., Zhu, Z., 2019. Current status of Landsat program, science, and applications. Remote Sens. Environ. 225 (November 2018), 127–147. http://dx.doi.org/10.1016/j.rse.2019.02.015.

Xiao, J., Chevallier, F., Gomez, C., Guanter, L., Hicke, J.A., Huete, A.R., Ichii, K., Ni, W., Pang, Y., Rahman, A.F., Sun, G., Yuan, W., Zhang, L., Zhang, X., 2019. Remote sensing of the terrestrial carbon cycle: A review of advances over 50 years. Remote Sens. Environ. 233 (January), 111383. http://dx.doi.org/10.1016/j.rse.2019.111383.

Yang, P., Prikaziuk, E., Verhoef, W., Van der Tol, C., 2020a. SCOPE 2.0: A model to simulate vegetated land surface fluxes and satellite signals. Geosci. Model Dev. Discuss. 2020, 1–26. http://dx.doi.org/10.5194/gmd-2020-251, URL: https://gmd.copernicus.org/preprints/gmd-2020-251/.

Yang, P., Van der Tol, C., 2018. Linking canopy scattering of far-red sun-induced chlorophyll fluorescence with reflectance. Remote Sens. Environ. 209, 456–467. http://dx.doi.org/10.1016/j.rse.2018.02.029.

Yang, P., Van der Tol, C., Yin, T., Verhoef, W., 2020b. The SPART model: A soil-plant-atmosphere radiative transfer model for satellite measurements in the solar spectrum. Remote Sens. Environ. 247 (May), 111870. http://dx.doi.org/10.1016/j.rse.2020.111870, URL: https://linkinghub.elsevier.com/retrieve/pii/S0034425720302406.

Yang, P., Verhoef, W., Prikaziuk, E., van der Tol, C., 2021. Improved retrieval of land surface biophysical variables from time series of sentinel-3 OLCI TOA spectral observations by considering the temporal autocorrelation of surface and atmospheric properties. Remote Sens. Environ. 256, 112328. http://dx.doi.org/10.1016/j.rse.2021.112328, URL: https://www.sciencedirect.com/science/article/pii/S0034425721000468.

Zhang, F., Chen, J.M., Chen, J., Gough, C.M., Martin, T.A., Dragoni, D., 2012. Evaluating spatial and temporal patterns of MODIS GPP over the conterminous U.S. against flux measurements and a process model. Remote Sens. Environ. 124, 717–729. http://dx.doi.org/10.1016/j.rse.2012.06.023.

Zhang, Y., Guanter, L., Berry, J.A., Joiner, J., van der Tol, C., Huete, A., Gitelson, A., Voigt, M., Köhler, P., 2014. Estimation of vegetation photosynthetic capacity from space-based measurements of chlorophyll fluorescence for terrestrial biosphere models. Global Change Biol. 20 (12), 3727–3742. http://dx.doi.org/10.1111/gcb.12664.

Zhang, K., Kimball, J.S., Running, S.W., 2016. A review of remote sensing based actual evapotranspiration estimation. Wiley Interdiscipl. Rev.: Water 3 (6), 834–853. http://dx.doi.org/10.1002/wat2.1168.

Zhang, Q., Xiao, X., Braswell, B., Linder, E., Baret, F., Moore III, B., 2005. Estimating light absorption by chlorophyll, leaf and canopy in a deciduous broadleaf forest using MODIS data and a radiative transfer model. Remote Sens. Environ. 99 (3), 357–371.

Zhou, H., Wu, D., Lin, Y., 2020. The relationship between solar-induced fluorescence and gross primary productivity under different growth conditions: Global analysis using satellite and biogeochemical model data. Int. J. Remote Sens. 41 (19), 7660–7679. http://dx.doi.org/10.1080/01431161.2020.1763507.